Sensitivity of Ocean Color Atmospheric Correction to Uncertainties in Ancillary Data: A Global Analysis With SeaWiFS Data

Frédéric Mélin, Paolo Colandrea, Pieter De Vis, and Samuel E. Hunt

***Abstract*— Atmospheric correction (AC) algorithms for ocean color (OC) data processing usually rely on ancillary data documenting the atmosphere and the sea state to help the calculation of the remote sensing reflectance R_{RS} from the radiance measured by a space sensor. This study aims at assessing the impact that the uncertainties associated with these ancillary data have on the AC outputs. For this objective, a full year of global Sea-viewing Wide Field-of-view Sensor (SeaWiFS) imagery is processed with the standard AC algorithm *l2gen* of the National Aeronautics and Space Administration with different sets of ancillary data, the reference case with National Centers for Environmental Prediction (NCEP) Reanalysis-2 meteorological data and satellite ozone products, as well as with ten ensemble members from the European Centre for Medium-Range Weather Forecast (ECMWF) CERA-20C data. The spread within the ensemble data and the differences with respect to the reference case are taken as a measure of the uncertainties associated with ancillary data. The impact on R_{RS} of perturbations in ancillary variables vary in space, the variables having the largest effects being wind speed and relative humidity, and ozone at bands where ozone absorption is largest, while sea-level pressure and precipitable water have the smallest effect. Sensitivity coefficients quantifying the relationship between perturbations in ancillary variables and effects on R_{RS} change with variable and wavelength. At the global scale, the variations found on R_{RS} when ancillary data are perturbed are usually small but not negligible and should be considered in the ocean color (OC) data uncertainty budget.**

***Index Terms*— Ocean color (OC), sea-viewing wide field-of-view sensor (SeaWiFS), uncertainties.**

I. Introduction

OCEAN color (OC) provides access to marine biological quantities, foremost the concentration of chlorophyll-a [1], a major and universal phytoplankton pigment. Other in-water quantities can be determined by OC remote sensing, e.g., in relation to sediment, dissolved organic matter or indicators of water quality [2]. Ultimately all OC in-water products are derived from the spectrum of reflectance characterizing the water body, expressed as remote sensing reflectance R_{RS} or water-leaving radiance L_w. This spectral quantity is recognized as an essential climate variable (ECV) by the Global Climate Observing System [3], as is the concentration of chlorophyll-a (Chl-*a*).

As with any geophysical product, R_{RS} data need to be accompanied by uncertainty estimates to allow an informed use of these data by the user community. Even though there is growing emphasis on the provision of uncertainties for satellite data [4], [5], this practice is in its infancy in the field of OC, which can be partly explained by the fact that this is particularly challenging: OC remote sensing is affected by a large and complex ensemble of error sources [6], including errors associated with the top-of-atmosphere (TOA) signal and the numerous assumptions and approximations needed to solve the remote sensing problem and find a solution for R_{RS}. This requires a proper metrological treatment of the OC data processing to model sources of uncertainties and their propagation in the various processing steps [7].

The remote sensing reflectance R_{RS} (or equivalently L_w) is obtained from the TOA signal L_t collected by the sensor in space through a process termed atmospheric correction (AC). The AC process is usually supported by ancillary (or auxiliary) information that documents the state of the atmosphere and sea surface as seen by the sensor. Appropriate quantities are typically provided by satellite products or reanalysis meteorological data given multiple times per day. These data have their own uncertainties that propagate through the AC algorithm and affect R_{RS}. This impact has been largely overlooked by the OC community, assuming that it was small. However, more solid knowledge is required to construct full uncertainty budgets for OC products. This issue is addressed here by exploiting the existence of ancillary data distributed by independent organizations, including ensemble datasets. In the absence of uncertainty estimates associated with each ancillary datum, it is assumed that variations within ensemble simulations and differences between products from independent organizations can be used as representations of uncertainties for testing purposes (as also discussed in [8]). In practice, the present study relies on the processing by a standard AC of Sea-viewing Wide Field-of-view Sensor (SeaWiFS) imagery at a global scale repeated for various sets of ancillary data to evaluate

Manuscript received September 9, 2021; revised December 18, 2021; accepted January 27, 2022. Date of publication February 9, 2022; date of current version March 24, 2022. This work was supported by the MetEOC-3 and MetEOC-4 projects through European Metrology Programme for Innovation and Research (EMPIR) under Grant 16ENV03 and Grant 19ENV07. EMPIR is co-financed by the Participating States and from the European Union's Horizon 2020 Research and Innovation Programme. *(Corresponding author: Frédéric Mélin.)*

Frédéric Mélin is with the Joint Research Centre, European Commission, 21027 Ispra, Italy (e-mail: frederic.melin@ec.europa.eu).

Paolo Colandrea is with Serco Italia S.p.a., 00044 Frascati, Italy.

Pieter De Vis and Samuel E. Hunt are with the National Physical Laboratory, Teddington TW11 0LW, U.K.

This article has supplementary downloadable material available at https://doi.org/10.1109/TGRS.2022.3150400, provided by the authors.

Digital Object Identifier 10.1109/TGRS.2022.3150400

TABLE I
LIST OF MAIN TERMS USED IN THIS ARTICLE

	Ancillary Data
WS	surface wind speed
SLP	sea level pressure
PW	precipitable water vapor
RH	relative humidity
$[O_3]$	total ozone concentration
$[NO_2]$	nitrogen dioxide concentration
	Terms in Atmospheric Correction Equations
L_t	Top-of-atmosphere radiance
L_r	Rayleigh radiance
L_a	aerosol radiance
L_w	water-leaving radiance
L_{WN}	normalized water-leaving radiance
L_g	radiance due to Sun glint
L_f	radiance due to white caps
T_v	sensor-path direct transmittance
$t_{d,v}$	sensor-path diffuse transmittance
$t_{d,s}$	solar-path diffuse transmittance
t_g	transmittance associated with gas absorption
R_{RS}	remote sensing reflectance
C_{BRDF}	BRDF correction
τ_a	aerosol optical thickness
α	Ångström exponent
	Statistical Terms
μ_{yr}	annual average
σ_{yr}	annual standard deviation
σ_{ens}	(quadratic) average ensemble spread
σ_{dif}	annual RMS difference between 2 variables
δ_{dif}	annual difference between 2 variables (bias)
$\partial Y/\partial x$	partial derivative of Y with respect to x
ΔY	gradient of Y

the resulting variations in terms of OC R_{RS} products. After having introduced the datasets and approach adopted for the analysis, global results are presented for various test cases. Then the sensitivity of the AC process to individual ancillary variables is discussed before conclusions are given.

II. DATA AND METHODS

Besides being introduced in the text, the main terms used in this article are listed in Table I.

A. Satellite Data

SeaWiFS level-1 global area coverage (GAC) data were obtained from the Ocean Biology Distributed Active Archive Center (OB.DAAC) of the National Aeronautics and Space Administration (NASA), Greenbelt, MD, USA, for the year 2003. They were processed to level-2 with the standard configuration of the *l2gen* AC of the SeaWiFS data analysis system (SeaDAS) [9] and remapped on a 12th-degree sinusoidal global grid (∼9 km in grid cell size) to get daily global maps. A specific dataset (subsequently referred to as the pixel dataset) is also assembled by accumulating all valid pixels (i.e., with valid AC outputs) of all level-2 images for four representative days in the year (15th of March, June, September, and December). Even though smaller than the 2003 daily level-three data (but with 3.7 million pixels distributed globally and across four seasons), it serves for pixel-based analyses that need to compare data before any averaging takes place (as happens with level-3 data).

B. Atmospheric Correction Algorithm

The *l2gen* standard AC algorithm [10], [11] requires a set of ancillary variables, including surface wind speed (WS), mean sea-level pressure (SLP), precipitable water vapor (PW), relative humidity (RH), total ozone concentration ($[O_3]$), and nitrogen dioxide concentration ($[NO_2]$). Both zonal and meridional components of WS are actually distinguished but only the modulus of the wind vector is used in the AC. Data of sea surface temperature and sea ice concentration are also requested but were not considered here as they do not directly impact the AC process. Local variations observed in $[NO_2]$ can have a significant impact on the AC [12]–[14] but they are found mostly in coastal regions [15]. In addition, *l2gen* relies on satellite products for $[NO_2]$, which are not available for the entire satellite OC record (and $[NO_2]$ is not distributed by CERA-20C). For these reasons, the processing carried out in this study used climatology values for $[NO_2]$ as the standard NASA processing. It is, however, acknowledged that a dedicated analysis of the impact of $[NO_2]$ focusing on coastal regions should be encouraged.

In this section, the main characteristics of the *l2gen* AC are recalled to ease the interpretation of the results. First, the radiative transfer problem is expressed by the following where L_t is a sum of contributions from L_w and the radiance associated with air molecules (Rayleigh radiance, L_r), aerosols (L_a), white caps or sea foam (L_f), and glint (L_g) [10], [11]:

$$L_t(\lambda) = t_{g,v}(\lambda)t_{g,s}(\lambda)\big[L_r(\lambda) + L_a(\lambda) + t_{d,v}(\lambda)L_w(\lambda) + t_{d,v}(\lambda)L_f(\lambda) + T_v(\lambda)L_g(\lambda)\big] \quad (1)$$

where $t_{d,v}$ and T_v are the diffuse and direct transmittance in the sensor-viewing direction [16], while absorption by gases (e.g., O_3 and NO_2) is written by the transmittance terms $t_{g,v}$ and $t_{g,s}$ for the paths from Sun-to-surface and surface-to-sensor, respectively. Note that in this equation, L_w is not the signal that would be actually measured in the field (as it does not include gaseous absorption occurring along the path Sun-to-surface). In the *l2gen* code implementation, this is corrected by having $t_{g,s}$ as denominator of L_w in (1), so that the *l2gen* L_w output (that can be saved in level-2 files) is comparable to that observed *in situ*. In (1), there is no term for correction of polarization effects as these are not considered for SeaWiFS, and corrections for out-of-band effects are not made explicit.

For further use in bio-optical algorithms, L_w goes through a process of normalization (*sensu* Gordon and Clark [17] and Morel and Gentili [18]) correcting for the path transmittance and bidirectional effects, and providing the normalized water

leaving radiance L_{WN} or remote sensing reflectance R_{RS}

$$R_{\mathrm{RS}}(\lambda) = \frac{L_{\mathrm{WN}}(\lambda)}{E_0(\lambda)} = \frac{L_w(\lambda, \theta_v, \theta_s, \phi)\ C_{\mathrm{BRDF}}(\lambda, \theta_v, \theta_s, \phi)^{-1}}{\cos\theta_s t_{g,s}(\lambda, \theta_s) t_{d,s}(\lambda, \theta_s) E_0(\lambda)(\bar{d}/d)^2} \tag{2}$$

where θ_s and θ_v are the solar and satellite zenith angles, respectively, and ϕ the relative azimuth between viewing and illumination direction; $t_{d,s}(\lambda)$ is the solar-path diffuse transmittance; d and $\bar{d}$ are the actual and average Earth–Sun distances, respectively. The correction for the bidirectional reflectance distribution function (BRDF) is written as

$$C_{\mathrm{BRDF}}(\lambda, \theta_v, \theta_s, \phi) = \frac{f(\lambda, \theta_s)}{Q(\lambda, \theta_v, \theta_s, \phi)} \frac{Q_0(\lambda)}{f_0(\lambda)} \frac{\Re(\lambda, \theta_v, \theta_s)}{\Re_0(\lambda)} \tag{3}$$

following [18], Q being the ratio between irradiance and radiance just below the water surface, f the ratio between irradiance reflectance and b_b/a (ratio of water backscattering and absorption coefficients), and $\Re$ being a function combining all reflection and refraction effects at the air-sea interface [18], [19]. In the *l2gen* code, the ratio f/Q is obtained from look-up tables (LUTs) [20] with a dependence on geometry and Chl-*a*, which means that it ultimately depends on all inputs to the code. $\Re$ is also dependent on geometry, and on WS for its above-to-below irradiance transmittance term, but this latter dependence is only seen for high solar zenith angles, above 60° [19].

For open ocean waters, where L_w in the near-infrared (NIR) can be assumed negligible following a black-pixel assumption [21], L_a can be computed knowing the other terms of (1). The ratio of the aerosol reflectance (converted into its single-scattering equivalent) at 765 and 865 nm (noted ϵ) can then be compared with tabulated values [10], [22]. The algorithm relies on 80 aerosol models [23] associated with eight values of RH (RH of 30%, 50%, 70%, 75%, 80%, 85%, 90%, and 95%) and ten values of the fraction (in volume) of the fine aerosol mode (from 0% to 95%). First, the two groups of aerosol models with RH bracketing the value obtained from the ancillary data are identified, and for each group, the two most appropriate models are selected on the basis of ϵ [10]. Ultimately, L_a can be computed in all bands by weighted averages from the four selected models.

This serves as the first step of an iterative process by which a possible contribution of L_w in the NIR is computed through a bio-optical model [24]. The contribution from L_w is then subtracted from L_t in the NIR bands leading to a new estimate of L_a, and the process starts again until convergence (or a maximum number of iterations) is reached. Therefore, for any perturbation affecting (1) at one band, L_w will not only be impacted at that band but also potentially at all other bands by this loop between visible and NIR wavelengths.

For the clarity of the discussion, it is worth introducing the various algorithmic modules where the ancillary data intervene.

1) *WS:* WS intervenes in various components of the algorithm. The radiance L_f due to white caps is a cubic function of WS for values between 6.33 and 12 m s^{-1} [25]: with WS below 6.33 m s^{-1}, L_f is considered negligible, while L_f for WS above 12 m s^{-1} reaches saturation. Since wind modifies the air-water interface geometry, it also has an effect on the glint radiance L_g [26], and on the computation of the Rayleigh radiance L_r [27]. As introduced earlier, WS is also found in the calculation of R_{RS} from L_w.
2) *SLP:* By modifying the Rayleigh optical thickness τ_r (proportional to SLP), SLP has an impact on the transmittance terms $t_{d,s}$, $t_{d,v}$, and T_v. The Rayleigh radiance L_r also depends on SLP [28].
3) *PW:* In the case of SeaWiFS, PW does not directly impact the gaseous transmittance terms. It has however an impact on the out-of-band corrections operating in the conversion between single and multiple scattering applied to aerosol reflectance.
4) *RH:* As explained earlier, RH is a major input to the algorithm as it modulates the selection of the aerosol models.
5) *[O_3]:* The concentration of stratospheric ozone has an exponential effect on the gaseous transmittance t_g.

C. Ancillary Data

Two independent sources of ancillary data were considered for the analysis. The first set relies on meteorological products (WS, SLP, PW, and RH) from National Centers for Environmental Prediction (NCEP), College Park, MD, USA, Reanalysis-2 data [29], [30] available every six hours on a 1° rectangular grid, and on satellite-derived [O_3] given on a daily basis on a 1.25° × 1° grid. For 2003, the latter is provided mainly from the Total Ozone Mapping Spectrometer (TOMS) and secondarily from the TIROS Operational Vertical Sounder (TOVS) for a few days (11) when TOMS data are not available [31]. In the rest of this article, this source of [O_3] data will be referred to simply as TOMS.

An alternative source of ancillary data was provided by the CERA-20C dataset from a coupled atmosphere–ocean assimilation system of the European Centre for Medium-Range Weather Forecast (ECMWF), Reading, U.K. To favor the coupling between ocean and atmosphere, surface field observations of pressure and marine wind were assimilated in the system [32]. Interestingly, CERA-20C (simply called CERA thereafter) comes in the form of a ten-member ensemble given every 3 h (i.e., ten realizations are provided for each variable and time step). The CERA-20C ensemble generation accounts for errors in observations assimilated in the reanalysis as well as model errors, and its spread can be seen as a measure of uncertainty even though it is likely an underestimate, possibly by a factor of 2 for some variables [32]. CERA-20C directly provides all ancillary data required for *l2gen*, except RH that was computed from 2-m surface temperature and 2-m dewpoint temperature [33] (the result can, therefore, be considered equivalent to NCEP RH given at 1000 hPa).

The spread of the CERA ensemble and the differences existing between the CERA data and the NCEP or TOMS data are taken as representative estimates of the uncertainties characterizing such ancillary data (see typical values of uncertainties in ancillary data in [6] and discussion in [8]). To drive *l2gen* with the CERA data (obtained on a 1° grid), the latter

is selected at the NCEP 6-h time steps for the meteorological variables, and bilinearly interpolated on the TOMS grid and averaged for the day for $[O_3]$ (the TOMS data being based on polar-orbiting satellite retrievals, a daily global map is not associated with a fixed time). Practically, NCEP or TOMS data were substituted in the files by the CERA equivalent data for easy ingestion within *l2gen*, where the values applied for each pixel are obtained by linear interpolation, in space (at the pixel location from the gridded ancillary data) and in time (from the ancillary data just before and after the satellite pass).

Besides the reference case based on the original NCEP and TOMS data, it was then possible to process the same SeaWiFS imagery using each member of an ensemble ancillary dataset, thus creating ensemble level-3 SeaWiFS data. In practice, global level-3 SeaWiFS data for 2003 were created 10 times in association with each ensemble member for the following cases.

1) *WS case:* Only WS is substituted by the ten members of the CERA data, keeping all other variables at their reference value (NCEP or TOMS).
2) *SLP case:* The same for SLP.
3) *PW case:* The same for PW.
4) *RH case:* The same for RH.
5) *[O_3] case:* The same for $[O_3]$.
6) *MET case:* only the meteorological variables WS, SLP, PW, and RH are substituted by the ten members of the CERA data, keeping $[O_3]$ at its TOMS value.
7) *ALL case:* All five variables are substituted by the ten members of the CERA data.

Adopting vocabulary typical of ensemble simulations, the ensemble variations of ancillary data that are input to *l2gen* will be termed perturbations.

For the cases where not all variables are perturbed, it is admitted that ancillary data are no longer strictly consistent (one variable coming from CERA and the others from NCEP/TOMS). However, the distributions provided by NCEP and CERA data are very similar (not shown) and the scope of the analysis is just to quantify the impact of small variations of each ancillary variable in terms of R_{RS} output.

D. Statistical Analysis

For a given variable x_j, average and standard deviation were computed over a year of data with the following expressions:

$$\mu_{yr} = \frac{1}{N_t}\sum_{j=1}^{N_t} x_j \tag{4}$$

$$\sigma_{yr} = \sqrt{\frac{1}{N_t - 1}\sum_{j=1}^{N_t}(x_j - \mu_{yr})^2} \tag{5}$$

where N_t is the number of time steps: when applied to ancillary data, N_t was the number of 6-h intervals for the meteorological data (4×365) and the number of days for $[O_3]$, whereas it was the number of valid daily level-3 values for OC products. While μ_{yr} provides the average level of a quantity, σ_{yr} is a measure of its natural variability.

For a given time step j and grid cell, average and standard deviation among the $N_{ens} = 10$ ensemble members $(x_{i,j})_{i=1,N_{ens}}$ (whether input ancillary data or output OC products) were computed as

$$\mu_j = \frac{1}{N_{ens}}\sum_{i=1}^{N_{ens}} x_{i,j} \tag{6}$$

$$\sigma_j = \sqrt{\frac{1}{N_{ens} - 1}\sum_{i=1}^{N_{ens}}(x_{i,j} - \mu_j)^2} \tag{7}$$

σ_j is the ensemble spread and represents a measure of the difference between the ensemble members. In order to obtain average estimates of the ensemble spread σ_j over the available time steps j of the year, a quadratic average σ_{ens} was computed as

$$\sigma_{ens} = \sqrt{\frac{1}{N_t}\sum_{j=1}^{N_t}\sigma_j^2}. \tag{8}$$

Therefore, σ_{ens} is an estimate of the average ensemble spread for the ancillary data or for the output level-3 SeaWiFS data.

Considering the NCEP/TOMS datasets as a reference x_{ref} (as reflecting the standard processing but without implying a higher quality), the differences between the average of the ensemble cases and the reference case were documented with the root-mean-square (RMS) difference σ_{dif} and the average difference δ_{dif} computed over the N_t available time steps

$$\sigma_{dif} = \sqrt{\frac{1}{N_t}\sum_{j=1}^{N_t}(\mu_j - x_{ref,j})^2} \tag{9}$$

$$\delta_{dif} = \frac{1}{N_t}\sum_{j=1}^{N_t}(\mu_j - x_{ref,j}). \tag{10}$$

Again, these statistics were computed for the input ancillary data or the output OC products. While σ_{ens} represents the average spread associated with the ensemble, σ_{dif} and δ_{dif} document the distance between CERA and NCEP/TOMS data, or between their associated OC outputs.

III. Global Analysis With Level-3 Data

A. Variations Within the CERA Ensemble

The impact of ensemble perturbations in ancillary data on the OC products is shown by Fig. 1 for the various cases where one variable is varied. These results pertain to the year 2003 but are very representative (similar results are obtained for other years as illustrated by the frequency distributions of the statistical quantities σ_{ens}, σ_{dif} and δ_{dif} shown for the ancillary data in Fig. 1 in the Supplementary Material). Fig. 1(a) and (b) shows the average ensemble spread σ_{ens} for WS (of global median 0.75 m s^{-1}, Fig. 1 in the Supplementary Material) and the resulting average spread for $R_{RS}(443)$, taken as a representative OC product [R_{RS} tend to show similar patterns, with various amplitudes, for all bands—see example at 555 nm in Fig. 2]. There is a clear relation between σ_{ens} of WS and $R_{RS}(443)$, with the largest values in the Southern Ocean (where σ_{ens} can exceed 1.5 m s^{-1} for WS) and secondary patterns in the northern Pacific Ocean

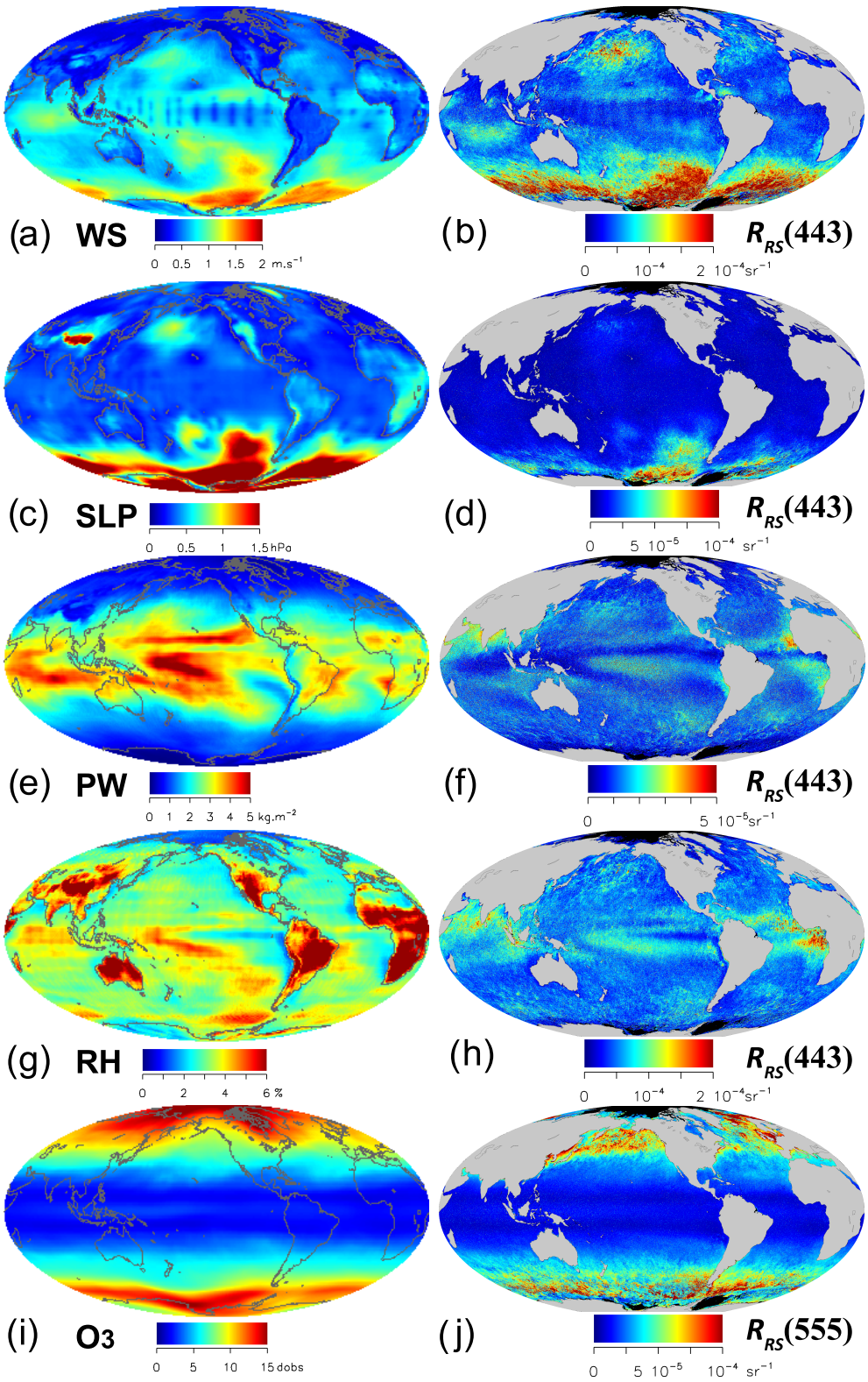

Fig. 1. Average ensemble spread σ_{ens} over 2003 for (a) WS, (c) SLP, (e) precipitable water PW, (g) RH, and (i) ozone [O_3], and the resulting average ensemble spread σ_{ens} for R_{RS} at (b), (d), (f), and (h) 443 and (j) 555 nm, when only the individual ancillary variable is perturbed. Gray indicates land masses or coast lines, while black is associated with the absence of valid values.

and southern Indian Ocean. Some relatively high values of σ_{ens} are seen for $R_{\text{RS}}(443)$ in the North Atlantic without a clear equivalent in WS. Distinct features seen in the equatorial Pacific and Atlantic Oceans for WS are likely the signatures of observational arrays [34], [35] that provide field data for assimilation in the CERA system (that to the contrary does not assimilate satellite data); related faint features can be noticed for $R_{\text{RS}}(443)$.

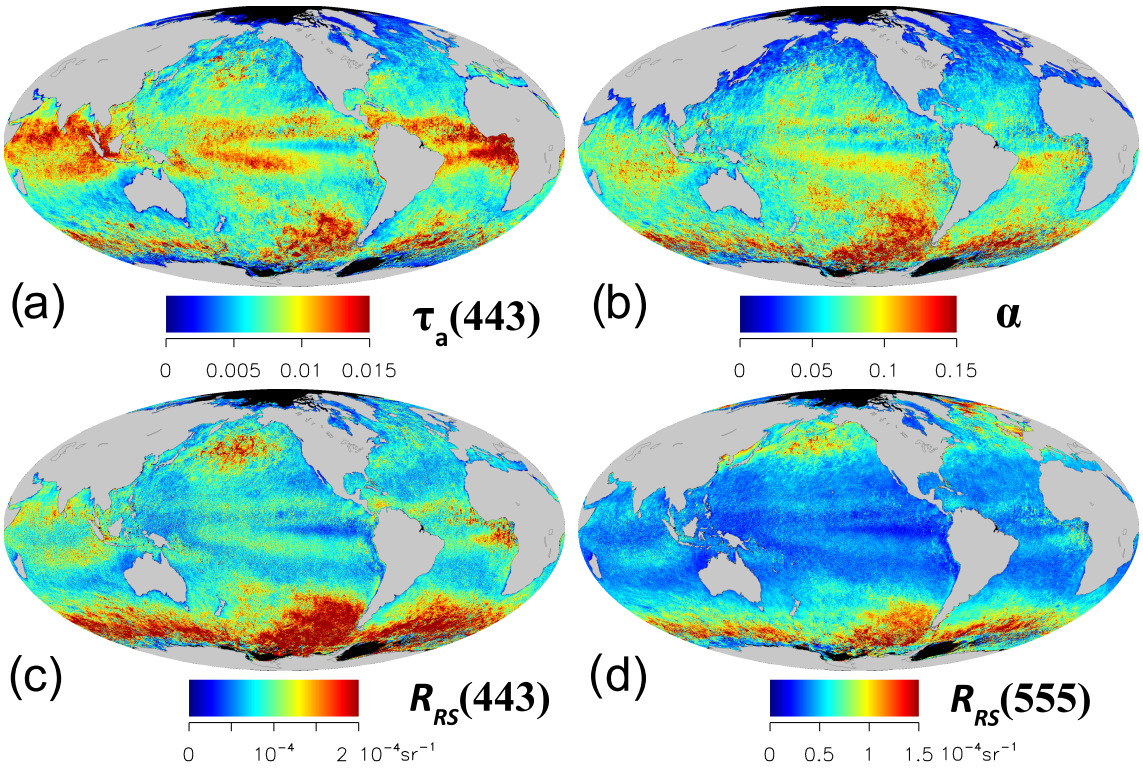

Fig. 2. Average ensemble spread σ_{ens} over 2003 when all five ancillary data are perturbed, for (a) $\tau_a(443)$, (b) α, (c) $R_{RS}(443)$, and (d) $R_{RS}(555)$. Gray indicates land masses, while black is associated with the absence of valid values.

The case of SLP is shown by Fig. 1(c) and (d) [notice the changes in color scale for $R_{RS}(443)$ in Fig. 1]: for SLP, σ_{ens} is most often below 0.5 hPa (global median 0.34 hPa, Fig. 1 in the Supplementary Material), with the highest values in the Southern Ocean (of the order of 1.5 hPa) and northwest Pacific. The resulting ensemble spread in $R_{RS}(443)$ is lower than in the WS case, with only small variations except in the Southern Ocean in agreement with large σ_{ens} found for SLP. Secondary patterns seen for SLP (like in the northwest Pacific Ocean) trigger only small responses in R_{RS}.

In general, σ_{ens} for R_{RS} is small when only PW is perturbed [Fig. 1(e) and (f)]. There is a general similarity between σ_{ens} of PW and R_{RS} in the tropical region where σ_{ens} is highest for PW; a local σ_{ens} minimum is observed for $R_{RS}(443)$ around the globe slightly north of the Equator, associated with relatively low σ_{ens} values for PW. The highest variations for R_{RS} are observed in the southeast Atlantic, and along the coasts of India and northwest Africa, without a corresponding signature for PW in the latter two cases. These regions are very challenging for the AC process because of clouds and aerosols and are associated with scarce OC data coverage so that a few cases might have a disproportionate impact on the annual average.

When only RH is perturbed, σ_{ens} for $R_{RS}(443)$ shows some similarity with RH's σ_{ens} [Fig. 1(g) and (h), with a RH global median of 3.2%]: for instance local minimum values in the Equatorial Pacific cold tongue with relatively high values in the equatorial western Pacific and Indian Oceans. More generally, σ_{ens} has relatively widespread medium values and shows a few features with extreme values. As in the case of PW, the coasts of India, northwest and equatorial Africa are characterized by high, relatively noisy, patterns of σ_{ens} for $R_{RS}(443)$ without an equivalent for RH.

For $[O_3]$, σ_{ens} (of global median 4.8 dobs) shows a clear gradient of increase with latitude, exceeding 10 dobs in the Southern Ocean [Fig. 1(i)]. The variations in terms of R_{RS} are not presented at 443 nm as the resulting σ_{ens} values are very small and fairly noisy (see its frequency distribution in Fig. 3). Differently, σ_{ens} for 555 nm shows a clear latitudinal gradient well consistent with that observed for $[O_3]$ [Fig. 1(j)]. Of course, the different impact on R_{RS} resulting from variations in $[O_3]$ is due to a different ozone absorption, 30 times higher at 555 nm than at 443 nm.

The average ensemble spread σ_{ens} in the ALL case (when all five ancillary data are perturbed) is given by Fig. 2 for the aerosol optical thickness τ_a at 443 nm, Ångström exponent α (characterizing the slope of $\log(\tau_a)$ between 510 and 865 nm), R_{RS} at 443 and 555 nm. The observed patterns are similar for these four products (as well as for other bands) even though with different relative amplitudes. For instance, regions of highest variations are seen in the Southern Ocean for R_{RS} with usually smaller values in the tropical oceans; to the contrary, high values of σ_{ens} are comparable for τ_a at low latitudes and in the Southern Ocean. Relatively low values are found for α in the high northern latitudes. Comparing Fig. 2 with Fig. 1, it can be seen that variations of WS contribute most in the northern Pacific and Atlantic Oceans and in the Southern Ocean, reinforced in that case by variations in SLP, whereas

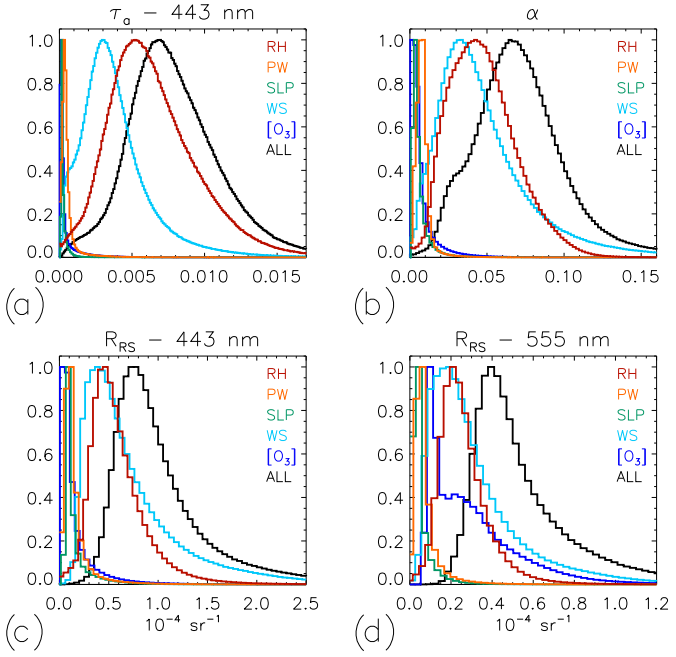

Fig. 3. Frequency distributions of average ensemble spread for (a) $\tau_a(443)$, (b) α, (c) $R_{RS}(443)$, and (d) $R_{RS}(555)$, for the case when all five ancillary data are perturbed (black line, "ALL") and for the cases where only one variable is perturbed.

variations in RH are felt mostly at low latitudes [compare Figs. 1(h) and 2(c)]. For wavelengths where ozone absorption is relatively high (e.g., at 555 nm), the impact of variations in $[O_3]$ is seen in the high latitudes.

These results can be summarized by Fig. 3 showing the frequency distributions for the various cases. This confirms that variations in WS and RH usually are by far the largest contributors to variations in the AC outputs. For R_{RS} at 443 nm, the median σ_{ens} is 0.901 in units of 10^{-4} sr^{-1} when all five ancillary data are varied [Fig. 3(c)]. When looking at individual cases with only one variable perturbed, the highest median is found for the WS case (0.569) closely followed by RH (0.539). Lower by a factor 5 is the PW case (0.119), whereas the SLP and $[O_3]$ cases have the lowest median σ_{ens} (0.089 and 0.084, respectively). As anticipated above, $[O_3]$ has a larger impact at bands with relatively high ozone absorption, such as 555 nm [Fig. 3(d)]: the median σ_{ens} is 0.25 10^{-4} sr^{-1} for the WS, RH and $[O_3]$ cases, approximately half the value obtained in the five-variable ALL case (0.479 10^{-4} sr^{-1}). Interestingly, the square root of the sum of the squares of the five σ_{ens} values obtained when perturbing one variable is usually close to σ_{ens} obtained when perturbing all five variables, which suggests that the effects are fairly uncorrelated; for instance, this RMS for $R_{RS}(443)$ is 0.802 10^{-4} sr^{-1} versus 0.901 10^{-4} sr^{-1} in the case of all five variables perturbed (0.432 versus 0.479 10^{-4} sr^{-1} at 555 nm).

B. Variations Between CERA and Reference Case

A similar analysis can be conducted about the impact on the OC products resulting from the differences between the CERA data and the reference dataset (NCEP and TOMS). As introduced in Section II-D, two metrics were used to document differences between datasets, the RMS difference σ_{dif} and the average difference δ_{dif}. As documented by Fig. 1 in the Supplementary Material, the differences between ancillary datasets, as quantified by σ_{dif}, are usually higher than the CERA ensemble spread (σ_{ens}) (the σ_{dif} global median is 1.64 $m\,s^{-1}$, 1.05 hPa, 5.1 kg m^{-2}, 8% and 20 dobs for WS, SLP, PW, RH, and $[O_3]$, respectively). Consequently, the differences observed between OC products when processed with CERA and NCEP/TOMS data are usually higher than differences observed for the ensemble spread, as can be seen by comparing Figs. 2 and 4 (note the change in color scales). For the sake of brevity, this section does not repeat for σ_{dif} the full analysis done on σ_{ens}; it merely shows σ_{dif} obtained when changing all five ancillary variables (Fig. 4), whereas it focuses on the impact of systematic differences between ancillary datasets on the OC products.

The distribution of σ_{dif} in general bears some resemblance with σ_{ens} but significant differences can be noted beside the generally higher values. For $\tau_a(443)$, patterns of high σ_{dif} are seen in various northern seas (Okhotsk, Bering, Labrador Seas, and Hudson Bay), in the Mediterranean Sea, and along the west African coasts, while the Southern Ocean does not stand out as for σ_{ens}. For the Ångström exponent α, σ_{dif} is rather more homogeneous than σ_{ens} [Fig. 4(b)]. The largest σ_{dif} for $R_{RS}(443)$ is seen at high latitudes and in some specific regions like the west African coasts [Fig. 4(c)]. The impact of WS is predominant in the northern Atlantic and Pacific Oceans (but not close to the coasts) and in the Southern Ocean, while variations in RH have the largest effect elsewhere (not shown). While the median σ_{dif} is 1.93 10^{-4} sr^{-1} when all five variables are changed, it is 1.02 and 1.27 10^{-4} sr^{-1} for the WS and RH cases, respectively. Despite the low resolution of the ancillary data, some local features can be noticed, like a high σ_{dif} associated with the wind regime in the Gulf of Tehuantepec (Pacific coast of Central America) [36]. At 555 nm, variations in WS and RH contribute to σ_{dif} in the same regions (see Fig. 2(a) in the Supplementary Material for σ_{dif} associated with the MET case) but variations of $[O_3]$ now have the largest impact on R_{RS}: with all five variables changed, the median σ_{dif} is 1.29 10^{-4} sr^{-1} while it is 0.42, 0.53, and 0.99 10^{-4} sr^{-1} for the WS, RH, and $[O_3]$ cases, respectively.

Differences between CERA and reference datasets have a systematic component at the scale of a year, the effect of which is seen as expressed by δ_{dif} in Fig. 5 for the five cases of individual variables being changed. It is recalled that δ_{dif} is positive (negative) when values associated with a CERA case are higher (lower) than the reference case. When only WS is substituted by CERA data, the resulting differences in $R_{RS}(443)$ follow fairly closely those seen for WS [Fig. 5(a) and (b)] but there are noticeable exceptions. For instance, areas of positive δ_{dif} for $R_{RS}(443)$ in the North Pacific are not obviously linked to patterns in WS. In the Indian sector of the Southern Ocean, δ_{dif} for WS is positive only far from the Antarctic continent which is not so for $R_{RS}(443)$. The feature observed in σ_{dif} in the Gulf of Tehuantepec is associated with a negative δ_{dif} for both WS and $R_{RS}(443)$.

In the SLP case [Fig. 5(c) and (d)], δ_{dif} is usually small for $R_{RS}(443)$ with higher values in the Southern Ocean that appear

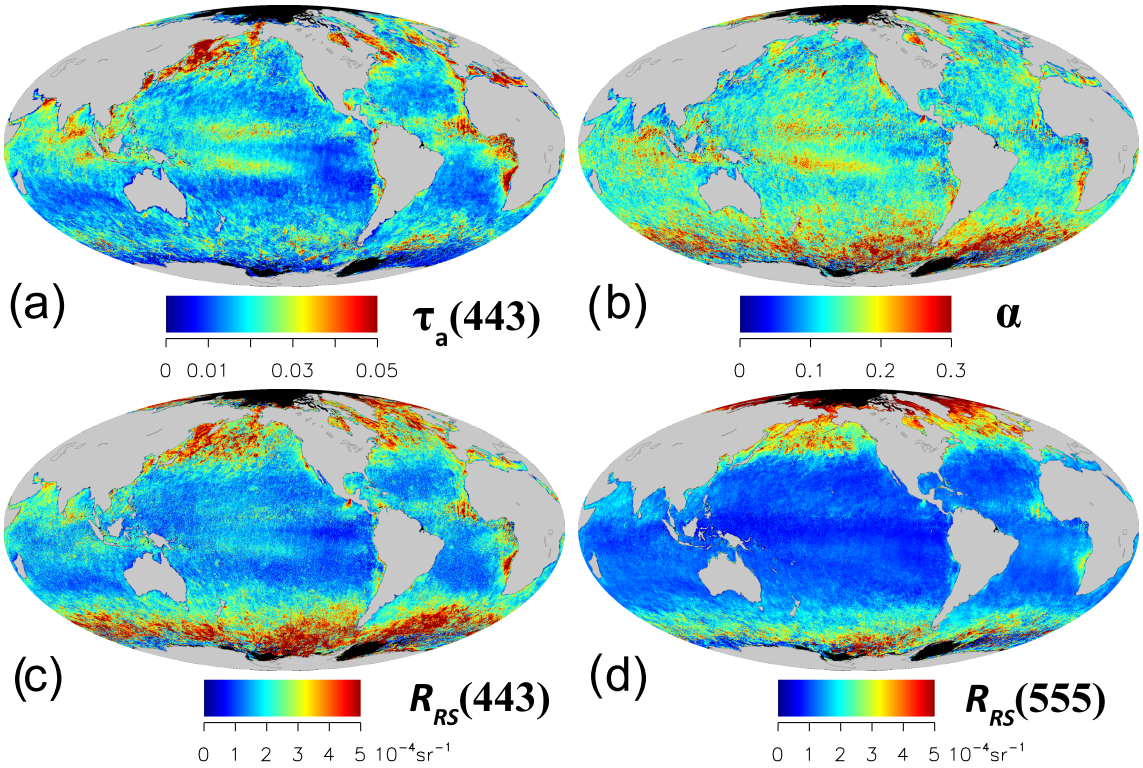

Fig. 4. RMS difference σ_{dif} over 2003 (ALL case) between the SeaWiFS products obtained with CERA data (averaged over the ensemble) and the SeaWiFS products obtained with reference ancillary data (NCEP and TOMS), for (a) $\tau_a(443)$, (b) α, (c) $R_{\text{RS}}(443)$, and (d) $R_{\text{RS}}(555)$. Gray indicates land masses, while black is associated with the absence of valid values.

negatively correlated with SLP's δ_{dif}. The impact of PW is weaker still [Fig. 5(e) and (f)], but some positive correlation can be seen in the equatorial regions: for instance negative δ_{dif} in the Pacific cold tongue region or equatorial Atlantic for both PW and $R_{\text{RS}}(443)$, and positive values in the Intertropical Convergence Zone (ITCZ).

Results in the RH case [Fig. 5(g) and (h)] show higher values of δ_{dif}. At low and mid-latitudes, δ_{dif} for RH and $R_{\text{RS}}(443)$ are mostly negatively related. Positive δ_{dif} for RH in the Indian Ocean, the tropical Pacific (except in its eastern part), or the Mediterranean Sea are associated with negative δ_{dif} for $R_{\text{RS}}(443)$; along the Atlantic African shores, δ_{dif} for RH is seen positive in the north and south and negative in the equatorial region, contrary to δ_{dif} for $R_{\text{RS}}(443)$. Negative δ_{dif} for RH in the mid-latitude ocean is also usually reversed for $R_{\text{RS}}(443)$. This inverse correlation is, however, not respected everywhere as can be seen in the Labrador Sea or the Hudson Bay. As for σ_{ens}, the $[O_3]$ case is illustrated at 555 nm [Fig. 5(j)]: a very clear correspondence is seen in δ_{dif} with a poleward gradient from negative to positive δ_{dif}, reflecting a strong impact of the differences in $[O_3]$ that exceed 20 dobs, particularly in the northern basins. Since these differences in $[O_3]$ appear high, it is mentioned here that the CERA-20C simulations do not include $[O_3]$ data in its assimilation scheme. Varying all meteorological data but not $[O_3]$ (MET case) leads to much lower δ_{dif} and a loss of the latitudinal gradient (see Fig. 2(b) in the Supplementary Material).

Fig. 6 shows δ_{dif} obtained in the ALL case (when all five ancillary variables are changed to the CERA data) for τ_a at 443 nm, α and R_{RS} at 443 and 555 nm. In general, δ_{dif} has the same sign for $\tau_a(443)$ and α even though there are exceptions (e.g., Okhotsk and Bering Seas, Hudson Bay) [Fig. 6(a) and (b)]. This is expected: for a given τ_a at 865 nm, τ_a at 443 nm will vary with α. For both aerosol products, the maps obtained for δ_{dif} are very close to those obtained when only RH is changed to CERA values (not shown). Also for both quantities, δ_{dif} at low latitudes is mostly positive (i.e., CERA-based data higher than the reference case) with some exceptions like the eastern Equatorial Atlantic and Pacific regions [Fig. 6(a) and (b)], following the difference in RH [Fig. 5(g)]. This relation is no longer obvious for high latitudes. In the open subtropical ocean, α is usually lower than 1 (e.g., [37]), corresponding to the candidate aerosol models of the AC having low fractions of the fine mode [23], and for these models, α tends to increase with RH, which is no longer true for higher fractions of the fine mode.

The signs of δ_{dif} tend to be opposite for $R_{\text{RS}}(443)$ and $\tau_a(443)$ (as variations in the aerosol radiance tends to compensate variations in R_{RS}) but this is not systematic [Fig. 6(a) and (c)]. Broadly speaking, for $R_{\text{RS}}(443)$, the effect of WS in terms of δ_{dif} are predominant in the Southern Ocean [following Fig. 5(b)], while variations in RH have the largest effect elsewhere, with secondary effects from PW (in low latitudes), SLP, and $[O_3]$. At 555 nm, δ_{dif} for R_{RS} mostly

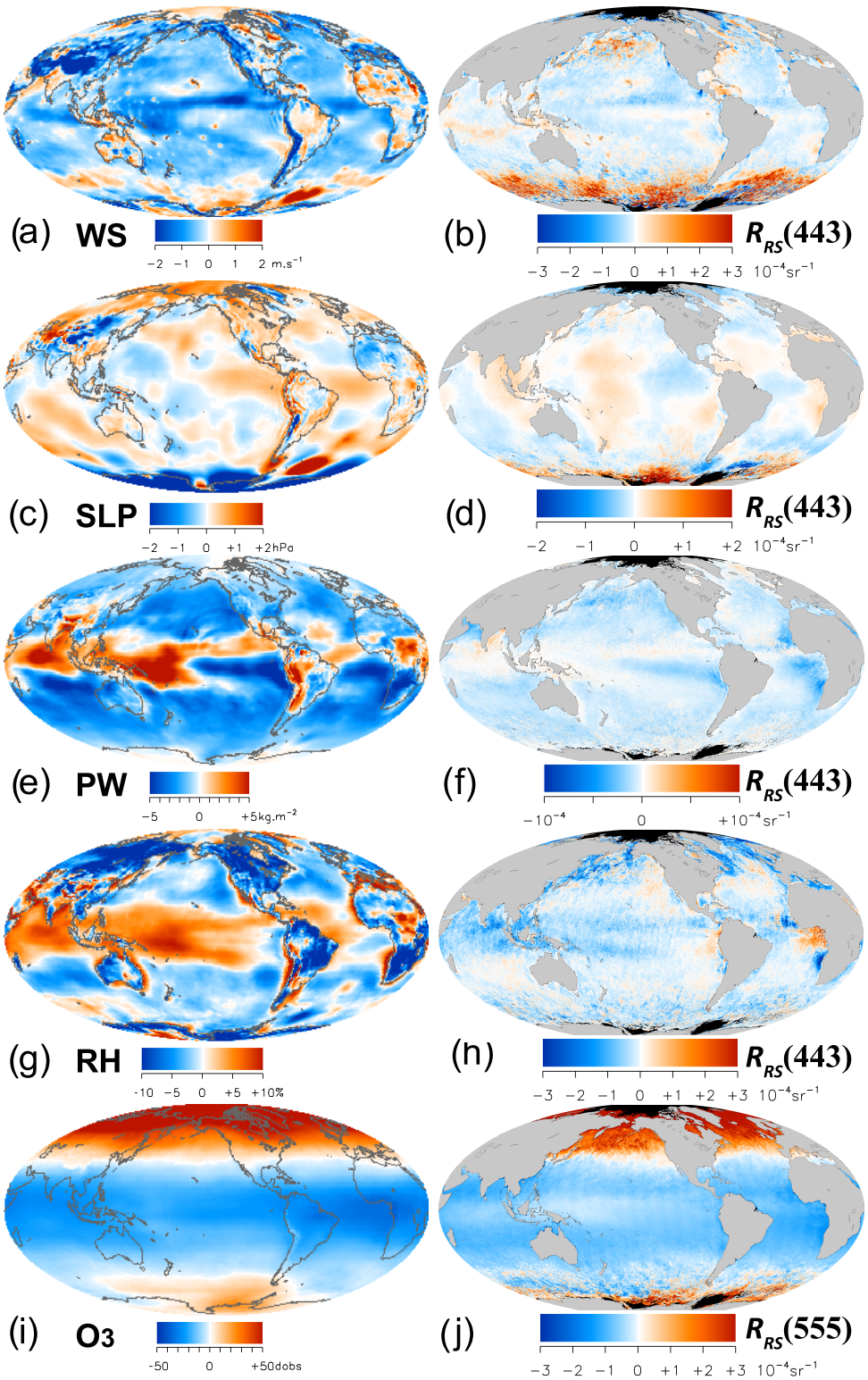

Fig. 5. Average difference δ_{dif} over 2003 between (a), (c), (e), and (g) CERA and NCEP data and (i) CERA and TOMS data, for (a) WS, (c) SLP, (e) precipitable water PW, (g) RH, and (i) ozone [O_3], and the resulting average difference δ_{dif} for R_{RS} at (b), (d), (f), and (h) 443 nm and (j) 555 nm, when only the individual ancillary variable is changed. Gray indicates land masses or coast lines, while black is associated with the absence of valid values.

bears the signature of [O_3] [compare Figs. 5(j) and 6(d)] with secondary influence from the other ancillary data.

C. Synthesis of Results

The preceding sections documenting the impact of variations in ancillary data on OC products show distinct patterns but their amplitude appears fairly small. In order to put these results in perspective, frequency distributions of various statistical indicators applied to R_{RS} are given in Fig. 7: annual average μ_{yr}, annual standard deviation σ_{yr}, σ_{ens} and σ_{dif}, allowing the comparison of the latter two indicators with the average level of R_{RS} and its average natural variability

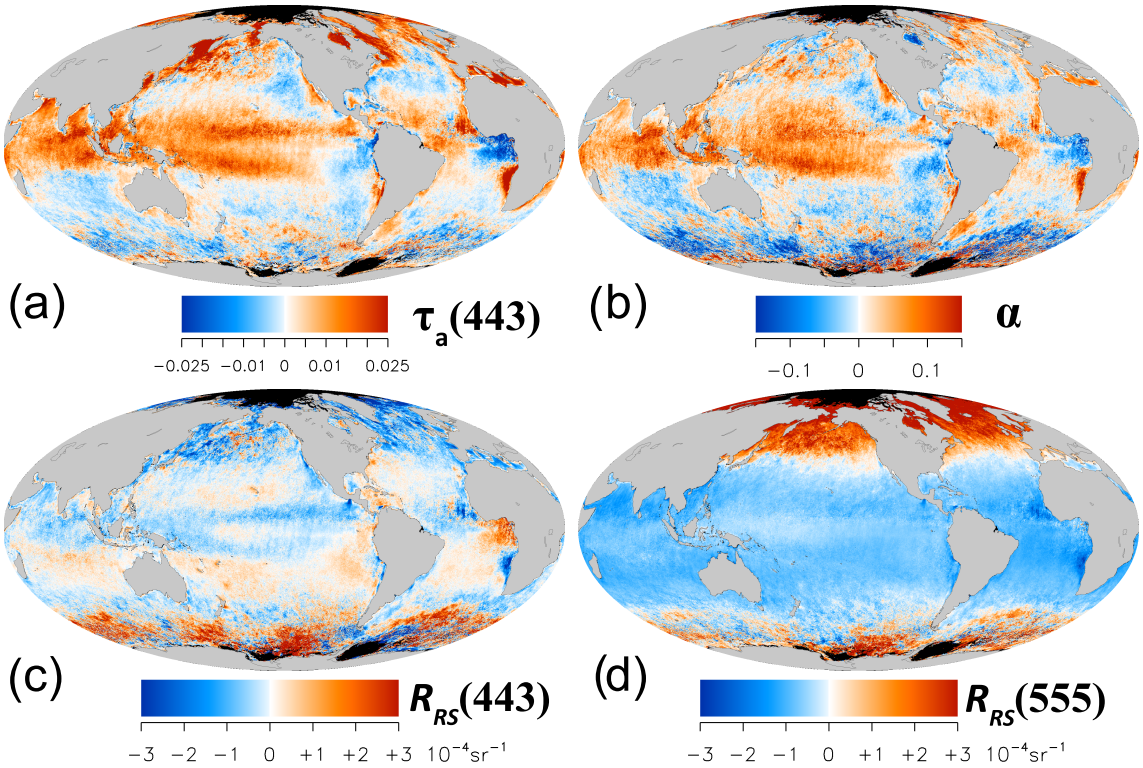

Fig. 6. Average difference δ_{dif} over 2003 (ALL case) between the SeaWiFS products obtained with CERA data (averaged over the ensemble) and the SeaWiFS products obtained with reference ancillary data, for (a) $\tau_a(443)$, (b) α, (c) $R_{\text{RS}}(443)$, and (d) $R_{\text{RS}}(555)$. Gray indicates land masses, while black is associated with the absence of valid values.

(see Fig. 1 in the Supplementary Material for statistics associated with ancillary data). First, the order of magnitude of the standard deviation of R_{RS} amounts to approximately a fifth of its annual average except at 670 nm where σ_{yr} is closer to μ_{yr} [in the global ocean, $R_{\text{RS}}(670)$ is usually small and its variations consequently tend to be high in relative terms]. As anticipated earlier, σ_{dif} is generally higher (by a factor ~ 2) than σ_{ens}. For completeness, it is mentioned that the OC products are stored as integers in level-2 files with a slope of 2 10^{-6} sr^{-1} for R_{RS} and 0.0001 for the aerosol products (τ_a or α), which quantifies the noise due to digitization of the data.

Reasoning in orders of magnitude with the global median of the ratios between the various statistical indicators, σ_{ens} is only $\sim$1.3% of μ_{yr} between 412 and 490 nm, but increases to 2.8% and 7% at 555 and 670 nm, respectively (Table II). Compared with the natural variability σ_{yr}, σ_{ens} amounts to 6%–12%. Looking at σ_{dif} instead, its median ratio with respect to μ_{yr} is 2.5%–4% between 412 and 510 nm, increasing to 7.6% and 16.1% at 555 and 670 nm, respectively. These median ratios are five times larger with respect to σ_{yr}, reaching 33% at 555 nm, a band for which R_{RS} average and variability are low in a large part of the ocean.

IV. Pixel-Based Analysis

Section III is based on annual statistics using level-3 data. While these provide general results, they do not allow a finer analysis that is instead possible with the pixel dataset.

TABLE II
GLOBAL MEDIAN RATIOS OF STATISTICAL INDICATORS FOR 2003 (EXPRESSED IN %)

wavelength (nm)	412	443	490	510	555	670
σ_{ens}/μ_{yr}	1.4	1.3	1.2	1.8	2.8	7.0
σ_{ens}/σ_{yr}	6.3	6.7	8.1	9.9	12.0	9.8
σ_{dif}/μ_{yr}	2.8	2.7	2.5	3.9	7.6	16.1
σ_{dif}/σ_{yr}	13.6	14.1	16.8	22.4	32.9	22.3

The first point that can be addressed with the pixel-based dataset is the importance of the selection of aerosol models. All ancillary data have, more or less directly, an impact on the radiance terms at 765 and 865 nm, and therefore, on the selection of the four aerosol models used in the AC for each pixel. The pixel dataset can be used to quantify how often the perturbations in ancillary data within the CERA ensemble result in a change in aerosol model selection (i.e., when at least one of the four models selected for the pixel is changed) for at least one ensemble member. When only WS, SLP, PW, RH, and [O_3] are perturbed using the CERA ensemble, a change in aerosol models happens for 32%, 7%, 15%, 84%, and 6% of the pixels, respectively. In all cases, σ_{ens} found for R_{RS} when a change in aerosol models occurs is on average higher than σ_{ens} without any change in model selection: for instance at 443 nm, σ_{ens} is higher by a factor that varies from 1.6 (for the SLP case) to 3.4 (for the RH case). The examination of individual images reveals that high variations can occur for isolated pixels due to a change in aerosol model selection

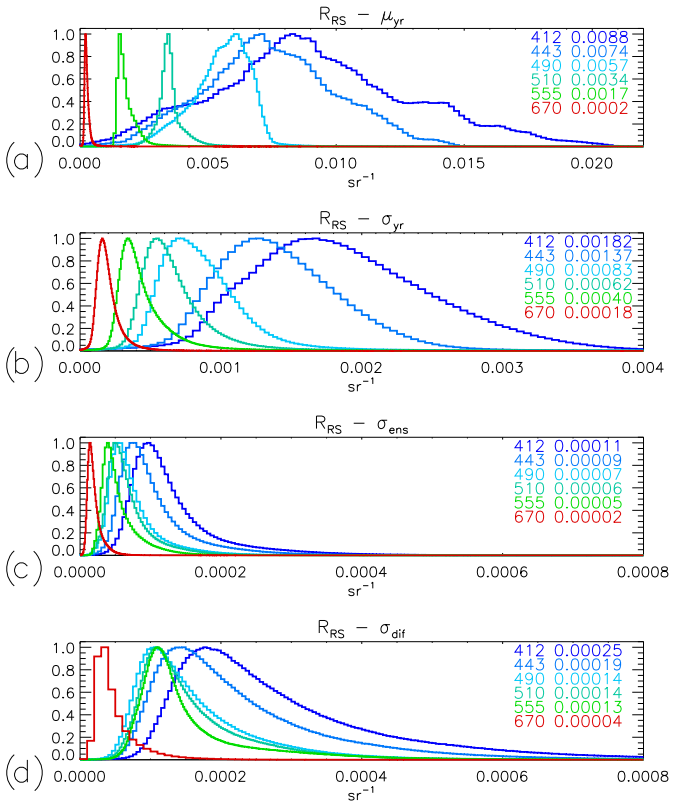

Fig. 7. For R_{RS} and the year 2003, frequency distributions (normalized by their maximum) of (a) the annual average μ_{yr}, (b) the standard deviation σ_{yr} (computed from daily data), (c) the average ensemble spread σ_{ens}, and (d) the RMS difference σ_{dif} between SeaWiFS data computed with CERA and reference ancillary data. For each distribution and SeaWiFS band, the median of the distribution is reported (in sr^{-1}). The scale for σ_{ens} and σ_{dif} is identical to allow an easy comparison.

triggered by one of the many factors having an influence on this selection (see examples in [8]).

A change in aerosol model selection has an impact on the whole visible spectrum and will tend to create the largest perturbations in R_{RS}. Not surprisingly, the RH case is associated with the highest incidence of change since RH has a direct action on the model selection, and RH is the variable having the largest weight in the ensemble spread observed for R_{RS} (Fig. 3). On average, WS is the second contributor to σ_{ens} and is also associated with a fairly high incidence of the aerosol model change. Even for the other variables, a change in aerosol model selection is not unusual. When all five ancillary data are perturbed, a change in aerosol models happens for 89% of the pixels, indicating that even the small variations in ancillary data observed in the CERA ensemble have a widespread impact on the functioning of the AC.

The pixel dataset also allows a direct, pixel-based, analysis of the relationships between differences in ancillary data and differences in OC products and tentative interpretations of the observed behavior. For this, each member of the CERA ensemble (for the cases where one ancillary variable is perturbed) is selected and compared with the reference dataset, since this offers a larger dynamic range than when comparing two members of the ensemble. Results are illustrated for R_{RS} at 443 nm (and at 555 nm for the $[O_3]$ case) by Fig. 8 in the form of scatter plots colored according to the density of points (complete results for all R_{RS} bands and aerosol products are shown in Figs. 3–8 in the Supplementary Material). The Pearson correlation computed on all (3.7 million) pairs is always significant ($p < 0.01$) for all variables (τ_a at 443 and 865 nm, α, and R_{RS}) for all five cases. However, the simple linear regression running on all points does not always appear representative of the average behavior of the data distributions, likely overly reacting to outliers (see Fig. 8). Therefore, differences in ancillary data first were binned and the median difference in the OC product was computed for each bin. Then, a linear regression was performed between the middle values of the bins associated with differences in ancillary data and the resulting median values of the differences in OC products. Only bins contributing to at least 1% of the dataset were considered (the black crosses in Fig. 8). The slopes of linear regression given in Table III are averages of slopes obtained over the ensemble when comparing each ensemble member and the reference case (coefficients of variation are given in the caption), while Fig. 8 is based on the first member of the ensemble for illustrative purposes (general results do not change with the choice of ensemble member). Values reported in Table III can be seen as representative estimates of the sensitivity coefficients $\partial R_{RS}/\partial x$ (where x is one ancillary variable) of the relationship between ancillary data and OC products. These estimates should, however, be treated with caution as there are sometimes large variations in this relationship (Fig. 8) and results might depend on the considered dataset.

A. Wind Speed

In general, in the WS case, $\tau_a(865)$ is barely affected, while $\tau_a(443)$ and α tend to decrease with WS (negative slope in Table III) and R_{RS} tends to increase in all bands [Fig. 8(a) and Fig. 3 in the Supplementary Material]. Equation (1) can be written as

$$L_t(\lambda) = t_{g,v}(\lambda)t_{g,s}(\lambda) \times \left[L_r(\lambda) + L_a(\lambda) + t_{d,v}(\lambda)L_f(\lambda) + T_v(\lambda)L_g(\lambda) + \cos\theta_s E_0(\lambda)t_{d,s}(\lambda)t_{d,v}(\lambda)R_{RS}(\lambda)\right] \quad (11)$$

by assuming the Sun at its mean distance and neglecting the BRDF effects for simplicity. As discussed in Section II-B, WS has a direct influence on L_r, L_f, and L_g, and an indirect impact on L_a through the influence on the former radiance terms in the NIR. WS is also found in the above-to-below irradiance transmittance term acting in the conversion between L_w and R_{RS} but with a small impact only seen for high solar zenith angles, typically above 60° [19]. Neglecting the impact on τ_a, and therefore, on the transmittance terms, partial differentiation of (11) with respect to WS (simply noted w) leads to

$$\frac{\partial R_{RS}}{\partial w} = \underbrace{-\frac{1}{\cos\theta_s E_0 t_d}\frac{\partial L_r}{\partial w}}_{[1]} \underbrace{-\frac{1}{\cos\theta_s E_0 t_d}\frac{\partial L_a}{\partial w}}_{[2]} \underbrace{-\frac{1}{\cos\theta_s E_0 t_{d,s}}\frac{\partial L_f}{\partial w}}_{[3]} \underbrace{-\frac{1}{\cos\theta_s E_0 t_d}\frac{\partial (T_v L_g)}{\partial w}}_{[4]} \quad (12)$$

TABLE III

ESTIMATES OF SENSITIVITY COEFFICIENTS USING BINNED DATA (SEE TEXT). FOR THE AEROSOL PRODUCTS (τ_a AND α), UNITS ARE IN $m^{-1}s$, hPa^{-1}, $kg^{-1}m^2$, $\%^{-1}$, AND $dobson^{-1}$ FOR THE CASES WS, SLP, PW, RH, AND [O_3], RESPECTIVELY. FOR R_{RS}, THE UNITS ARE THE SAME MULTIPLIED BY sr^{-1}. VALUES ARE AVERAGES COMPUTED USING THE TEN ENSEMBLE MEMBERS. FOR R_{RS} IN THE WS CASE, THE COEFFICIENT OF VARIATION (CV, RATIO OF STANDARD DEVIATION AND AVERAGE) IS BETWEEN 2.1% AND 5.8% (AND 14% AT 670 nm). IN THE SLP CASE, CV IS LOWER THAN 1.2% FOR WAVELENGTHS BETWEEN 412 AND 555 nm. CV IS BETWEEN 3% AND 4% FOR THE PW CASE. FOR THE RH CASE, IT IS 10%–13% (BUT 43% AT 670 nm). FOR THE [O_3] CASE, CV IS IN THE INTERVAL 2.6%–3.2%. NO VALUES ARE PROVIDED WHEN VARIATIONS ARE OBVIOUSLY TOO CLOSE TO THE DIGITIZATION LIMITS ASSOCIATED WITH THE STORING OF THE DATA (SEE THE SUPPLEMENTARY MATERIAL FOR THE COMPLETE SET OF SCATTER PLOTS)

	$\tau_a(443)$	$\tau_a(865)$	α	412	443	490	510	555	670
WS	-9.2 10^{-4}	-1.4 10^{-4}	-4.8 10^{-3}	4.6 10^{-5}	3.0 10^{-5}	1.5 10^{-5}	1.1 10^{-5}	5.8 10^{-6}	1.1 10^{-6}
SLP	-5.1 10^{-4}	-	-6.5 10^{-3}	-4.1 10^{-5}	-2.7 10^{-5}	-1.4 10^{-5}	-1.1 10^{-5}	-5.5 10^{-6}	-
PW	-5.9 10^{-5}	2.5 10^{-5}	-1.8 10^{-3}	2.4 10^{-6}	2.0 10^{-6}	1.6 10^{-6}	1.4 10^{-6}	1.0 10^{-6}	5.7 10^{-7}
RH	1.1 10^{-3}	3.4 10^{-4}	3.7 10^{-3}	-5.5 10^{-6}	-3.9 10^{-6}	-2.3 10^{-6}	-1.7 10^{-6}	-9.3 10^{-7}	-6.6 10^{-8}
$[O_3]$	2.4 10^{-5}	-1.3 10^{-6}	3.7 10^{-4}	-1.4 10^{-6}	-9.7 10^{-7}	1.4 10^{-6}	3.3 10^{-6}	5.5 10^{-6}	1.1 10^{-6}

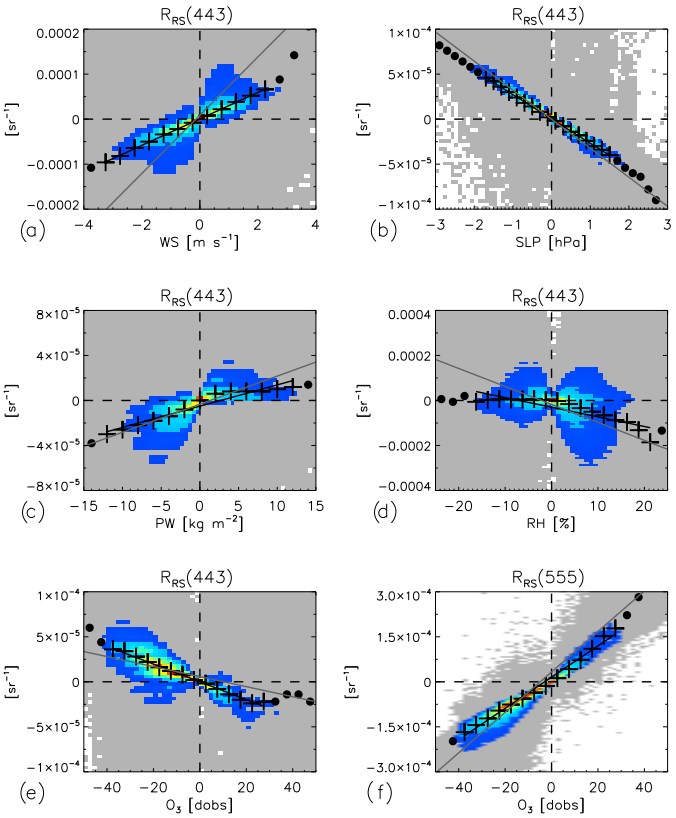

Fig. 8. Scatter plots of differences in R_{RS} (a)–(e) at 443 nm and (f) 555 nm versus differences in meteorological data (CERA—NCEP) for (a) WS, (b) SLP, (c) PW, (d) RH, or (e) and (f) ozone data [O_3] (CERA—TOMS). Colors go from blue to red with an increasing density of points, with light gray associated with the 2-D bins of the scatter plots contributing less than 1% of the maximum density. The gray line represents the linear regression performed over all points. Dots and crosses represent a 2-D binning of the distribution (see text), with dots associated with bins with less than 1% of the data. The black line shows the linear regression using the binned data with only bins accounting for more than 1% of the data (crosses).

by noting t_d the product $t_{d,s}t_{d,v}$. The importance of each term can be quantified by approximating $\partial Y/\partial w$ by $\Delta Y/\Delta w$, where Y is any of the relevant variable (e.g., R_{RS}), Δw is the difference in WS between the CERA and NCEP values and ΔY the resulting difference for Y. Only pixels for which $\Delta w \geq 0.5$ m s^{-1} (66% of the total number of pixels) are considered (to avoid too small differences for numerical reasons). Fig. 9 shows the various terms of (12) with associated median $\Delta R_{RS}/\Delta w$. First, it is worth noting that the observed distribution of $\Delta R_{RS}/\Delta w$ is consistent with the slope reported in Table III [compare the first line of Table III with the median values of $\Delta R_{RS}/\Delta w$ in Fig. 9(a)]. Let us first consider the term [4]. For 73% of the analyzed pixels ($\Delta w \geq 0.5$ ms^{-1}), ΔL_g is equal to 0 at all bands, which is explained by the fact that the glint correction only operates in the algorithm for glint conditions retained as moderate [38]. The remaining values are widely spread (mostly positive, leading to [4] being negative) without showing distinct patterns (so that [4] is not included in Fig. 9). For example at 412 nm, [4] has a median of $-0.94\ 10^{-4}$ sr^{-1}m^{-1}s when it is not null, which means that the impact of WS through the glint radiance can be significant for individual pixels.

The radiance due to white caps L_f increases as a cubic function of WS, which might decrease R_{RS} in the radiance budget of (11), everything else being assumed equal. The term [3] is equal to $-1/\pi\,\partial\rho_f/\partial w$ where ρ_f is the white cap reflectance. For 55% of the analyzed pixels, the term [3] is null at all bands: L_f is equal to 0 when WS is lower than 6.33 ms^{-1}, while for winds higher than 12 ms^{-1}, the effects of WS do not operate as the calculation of L_f saturates above this value. For medium WS, the term [3] remains anyway very small, tailing from 0 toward the negative values as expected [Fig. 9(d)].

Even though only slightly and not systematically, L_r tends to decrease with WS in the blue (favoring an increase in R_{RS}), a behavior that tends to be reversed for higher wavelengths [27], leading to the distributions observed for the term [1] in Fig. 9(b). These effects are reinforced with high solar zenith angles, so more frequently in high latitude regions (which is consistent with the geographical patterns seen in Fig. 1(b). It is the term [2] related to $\Delta L_a/\Delta w$ that has the largest weight in defining the distribution of $\Delta R_{RS}/\Delta w$ [compare Fig. 9(a) and (c)]. This action originates in the NIR in three ways related to L_f, L_g, and L_r. In the NIR, where L_w is usually very small, an increase of L_f with WS tends to decrease L_a, a change that is propagated across the visible

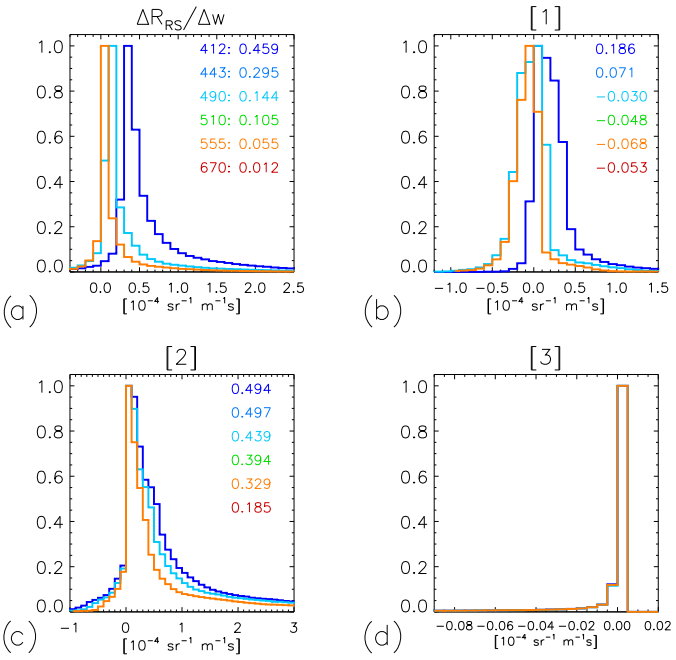

Fig. 9. Frequency distributions (normalized by their maximum) of the terms associated with (12): (a) $\Delta R_{\rm RS}/\Delta w$, (b) [1], (c) [2], and (d) [3]. Median values are indicated for the six wavelengths [listed in panel (a)] in units of 10^{-4} $\rm sr^{-1}m^{-1}s$, except for [3] where all median values are null. To allow readability, only the distributions for 412, 490, and 555 nm are shown. For [3], they are in practice superimposed.

domain. In addition, the white cap reflectance decreases with wavelength in the NIR [39] so that a higher L_f leads to a lower ϵ (ratio of aerosol reflectance), again leading to lower L_a values in the visible bands. The pixel dataset was also created removing the correction for white cap reflectance, and the results are comparable with those observed in Fig. 8(a) (or Fig. 3 in the Supplementary Material), with a distribution of points closer to the regression line (not shown), indicating that the impact of L_f is small, either through the term [3] or through its action on L_a. In the same way, variations in L_g affect L_a in the NIR, and therefore, across the spectrum. Another pixel dataset was generated removing the corrections for white cap reflectance and for the glint, leading to a distribution of points again comparable to the case with both corrections but still closer to the regression line (see Fig. 4 in the Supplementary Material). Therefore, the term [2] mostly comes from the variations of L_r in the NIR, generally leading to a decrease of L_a across the spectrum [and a term [2] usually positive, Fig. 9(c)].

In conclusion, $\Delta R_{\rm RS}/\Delta w$ is largely the result of changes of L_r at the considered wavelength and through their actions on L_a in the NIR, with a decreasing amplitude for higher wavelengths (see slopes in Table III). This primary effect of WS is perturbed for some pixels by the actions of L_f and L_g (terms [3] and [4]), which are negative at a given visible wavelength but are indirectly compensated through the NIR by their actions on L_a. These indirect actions actually seem to be prevalent as the observed sensitivity factor $\partial R_{\rm RS}/\partial w$ is lower when L_f and L_g are ignored in the AC process. For instance, the slope for $R_{\rm RS}(443)$ associated with the first ensemble member [Fig. 8(a)] is 2.9 10^{-5} $\rm sr^{-1}m^{-1}$ s; removing the impact of white caps, this slope becomes 2.5 10^{-5} $\rm sr^{-1}m^{-1}$ s, and 2.4 10^{-5} $\rm sr^{-1}m^{-1}$ s when white caps and glint are neglected.

B. Sea-Level Pressure

In the SLP case, there is a clear negative relationship between the OC products (for both aerosol and $R_{\rm RS}$) with fewer outliers compared with the other cases, so that the slopes of linear regression computed on all data and on binned data are similar. The amplitudes of changes are, however, small [see Fig. 1(d) and (b) and Fig. 5 in the Supplementary Material], with variations close to the digitization levels for $R_{\rm RS}(670)$ and $\tau_a(865)$ (2 10^{-6} $\rm sr^{-1}$ and 0.0001, respectively) so that no sensitivity factors are given for these quantities in Table III.

An increase of L_r in the NIR due to SLP might lead to a decrease in L_a in the NIR, and thus, across the spectrum, favoring an increase in $R_{\rm RS}$. In addition, the relative increase of L_r with SLP changes very little with wavelength, so that for a given SLP increase, L_r will increase more at 765 nm than at 865 nm (L_r being higher at the former wavelength), so that L_a will be relatively more depressed at 765 nm, decreasing ϵ and again L_a at all bands. This is consistent with the negative regression slopes found for $\tau_a(443)$ and α (Table III). However, the most direct impact of a change in SLP is a change of the same sign for L_r [27], leading to an opposite change in L_w and $R_{\rm RS}$. For a given wavelength and everything else being equal, a higher SLP also leads to lower $t_{d,v}$ and $t_{d,s}$, and consequently higher $R_{\rm RS}$ [since their product appears in (11)]. These contrasting impacts can be written at a given wavelength in the following way, neglecting BRDF effects and assuming a mean Sun–Earth distance, with partial differentiation with respect to SLP [noted p in (13)]

$$\frac{\partial R_{\rm RS}}{\partial p} = \underbrace{-\frac{1}{\cos\theta_s E_0 t_d}\frac{\partial L_r}{\partial p}}_{[1]} \underbrace{-\frac{1}{\cos\theta_s E_0 t_d}\frac{\partial L_a}{\partial p}}_{[2]} \underbrace{-\frac{\partial t_d}{\partial p}\frac{R_{\rm RS}}{t_d}}_{[3]}. \quad (13)$$

In that case, there is no dependence of L_f and L_g on SLP. Fig. 10 shows the distribution of the various terms of (13) in the approximate form $\Delta Y/\Delta p$ for $\Delta p \geq 0.5$ hPa. Again, the median values obtained for $\Delta R_{\rm RS}/\Delta p$ are in excellent agreement with the slope of linear regression obtained on the binned data given in Table III. The distributions of $\Delta R_{\rm RS}/\Delta p$ are fairly narrow with some tails toward more negative values, which is consistent with the distribution of points along the regression line in Fig. 8(b) (or Fig. 5 in the Supplementary Material). In (13), the term [3] (that can be written as $+\tau_r/2{\rm AM}/p_0 R_{\rm RS}$ with τ_r the Rayleigh optical thickness, AM the air mass equal to $1/\cos\theta_s + 1/\cos\theta_v$, and p_0 the standard SLP of 1013.25 hPa) is approximately an order of magnitude lower than the other terms (Fig. 10). The main term is term [1] associated with the direct effect of L_r on $R_{\rm RS}$, that is partly compensated by the term [2] (indirect effect of L_r on L_a), leading to the remarkable relationship seen in Fig. 8(b) (and Fig. 5 in the Supplementary Material).

C. Precipitable Water

There is a larger variability in the PW case [Fig. 8(c) and Fig. 6 in the Supplementary Material], with a generally

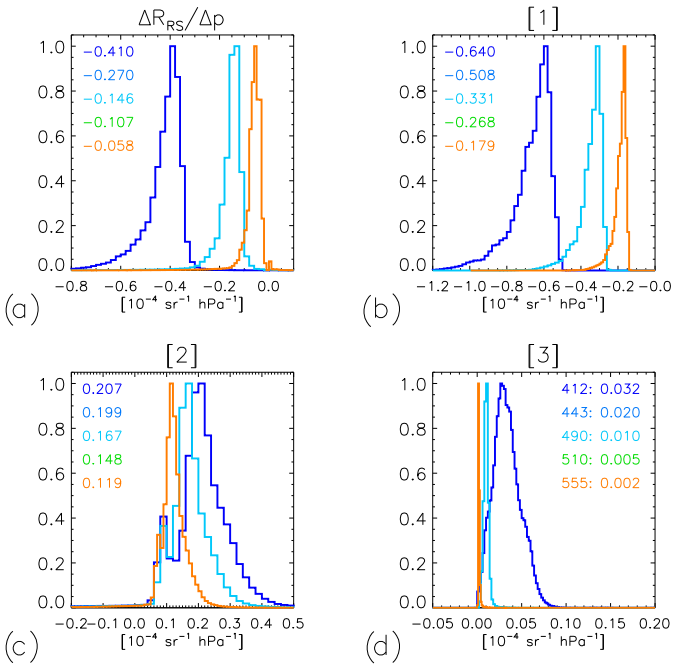

Fig. 10. Frequency distributions (normalized by their maximum) of the terms associated with (13): (a) $\Delta R_{RS}/\Delta p$, (b) [1], (c) [2], and (d) [3]. Median values are indicated for five wavelengths [listed in (d)] from 412 to 555 nm, in units of 10^{-4} sr^{-1} hPa^{-1} (ΔR_{RS} being close to the digitization level at 670 nm). To allow readability, only the distributions for 412, 490, and 555 nm are shown.

positive relationship between differences in PW and in R_{RS}. The slope is also slightly positive for τ_a at 865 nm, but becomes negative at 443 nm and for α (Table III). These results are consistent with a slight increase of L_a at 865 nm, associated with a decrease of ϵ, and therefore, of L_a across the visible bands, ultimately leading to an increase in L_w or R_{RS} (Table III). This action operates predominantly in the NIR bands for which water vapor absorption becomes more significant (e.g., [40]). As anticipated in Section II-B, PW affects out-of-band corrections performed in multiple-to-single and single-to-multiple scattering conversions of the aerosol reflectance, and a deeper understanding of the mechanisms at play would require a dedicated study. It is anyhow recalled that the impact of PW (within the range of values tested) is small among the five cases considered in this study.

D. Relative Humidity

The frequency distributions found for the RH case do not show a linear pattern even though the relationship tends to be slightly negative for R_{RS} and positive for the aerosol products [Table III, Fig. 8(d) and Fig. 7 in the Supplementary Material]. As described in Section II-B, the calculation of the aerosol reflectance in the visible is performed as a weighted average of contributions from (up to 4) aerosol models, and the position of the observed RH with respect to the eight tabulated values (30%, 50%, 70%, 75%, 80%, 85%, 90%, and 95%) defines the weights given to the models associated with values bracketing RH. If RH moves across a tabulated value, the selected aerosol models are changed, which introduces a divergence in the calculations of L_a. This happens more often for high RH as the steps in tabulated values become finer (5%), an aspect which is not really relevant as RH over the oceans is mostly above 70% [8]. The ultimate effect on the AC of a change in RH depends, among other things, on the selected aerosol models and their associated fine-mode fraction. For instance, the Ångström exponent α usually increases with RH for low fractions (below 0.3), and therefore, low α, while it decreases for high fractions (above 0.8) and high α. The results of Table III merely suggests that the former scenario happens more often, which is consistent with the fact that most of the open ocean, at least in low-to-mid latitudes, is characterized by α not exceeding 1 [37], [41], [42].

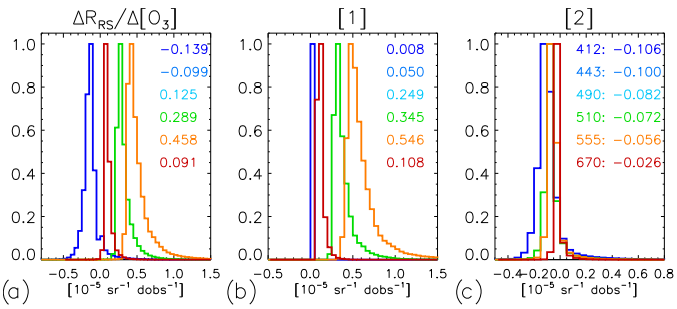

Fig. 11. Frequency distributions (normalized by their maximum) of the terms associated with (15): (a) $\Delta R_{RS}/\Delta O_3$, (b) [1], and (c) [2]. Median values are indicated for the six wavelengths [listed in (c)] in units of 10^{-5} sr^{-1} dobs^{-1}. To favor readability, only the distributions for 412, 510, 555, and 670 nm are shown.

E. Ozone Concentration

In the [O_3] case, there is not much impact of the differences in ancillary data for $\tau_a(865)$ but a larger, positive, slope for α and $\tau_a(443)$ is seen (Table III, Fig. 8 in the Supplementary Material). For R_{RS}, the slope is found negative at 412 and 443 nm but becomes increasingly positive between 490 and 555 nm [Fig. 8(e) and (f)] and is still positive at 670 nm. Neglecting the impact of NO_2, gaseous transmittance t_g (the product of $t_{g,s}$ and $t_{g,v}$) for SeaWiFS bands is $e^{-\tau_{O3}.AM}$ with τ_{O3} the optical thickness due to ozone, i.e., the product of [O_3] and the absorption coefficient k_{O3}. Again, the effect of variations in [O_3] on R_{RS} can be seen as the sum of a direct effect through t_g, and an indirect effect through the NIR on L_a, leading to the following differentiation:

$$L_t \frac{\partial(1/t_g)}{\partial O_3} = \cos\theta_s E_0 t_d \frac{\partial R_{RS}}{\partial O_3} + \frac{\partial L_a}{\partial O_3} \tag{14}$$

which can be rewritten as

$$\frac{\partial R_{RS}}{\partial O_3} = \underbrace{\frac{k_{O3}.AM}{\cos\theta_s E_0 t_d t_g} L_t}_{[1]} \underbrace{- \frac{1}{\cos\theta_s E_0 t_d} \frac{\partial L_a}{\partial O_3}}_{[2]}. \tag{15}$$

Fig. 11 shows the distributions of these terms in the approximate form $\Delta R_{RS}/\Delta O_3$, the median values of which are comparable to the slope of linear regression obtained on the binned data given in Table III. For a given L_t detected by the sensor, a larger [O_3] increases the value of the TOA radiance that is input to the AC after correction for gaseous transmittance. In the visible bands, everything else being assumed equal, this

is translated into an increase in R_{RS} in a manner proportional to ozone absorption [Fig. 11(b)]. In the NIR (where L_w is very small), this same effect instead leads to an increase in L_a, a change that is relatively higher at 765 nm (O_3 absorption being 2.44 times higher at 765 nm than at 865 nm), both effects that tend to increase L_a at all visible bands (as well as α and τ_a) and decrease L_w. Therefore, when the ozone absorption is small such as at 412 or 443 nm, the term [2] dominates and the sensitivity factors $\partial R_{RS}/\partial O_3$ are negative. When ozone absorption increases, the opposite effect is seen, for instance at 555 nm where term [1] becomes an order of magnitude higher than term [2], leading to a largely positive sensitivity factor, 5.5 10^{-6} sr^{-1} $dobs^{-1}$.

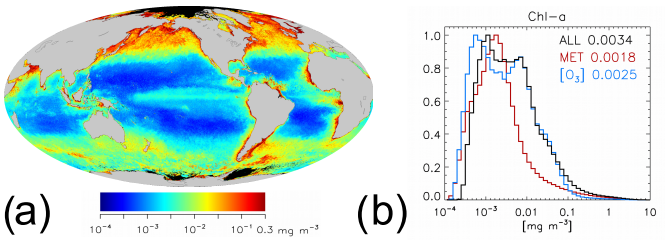

Fig. 12. (a) Average ensemble spread σ_{ens} for Chl-*a* over 2003 when all five ancillary variables are varied; gray indicates land masses, while black is associated with the absence of valid values. (b) Frequency distributions of σ_{ens} for Chl-*a* and associated global median (in mg m^{-3}), when all ancillary data are varied (ALL case, in black), when only the meteorological data are varied (MET case, in red), and when only $[O_3]$ is varied ($[O_3]$ case, in blue).

V. Discussion and Conclusion

This study aimed at quantifying the impact of uncertainties of ancillary data on the outputs of a standard AC algorithm. Of course, the results are applicable only for the considered algorithm (*l2gen*) and for SeaWiFS, but they are expected to hold in general terms for other multispectral sensors when processed by *l2gen* since the bands are similar and the physical relationships underpinning the algorithms are identical. They might have a more general validity at least in terms of orders of magnitude and/or signs of the impact. Indeed other AC codes based on various algorithmic approaches rely on LUTs for Rayleigh radiance calculations (for which a similar dependence on atmospheric pressure and WS is usually included), model a contribution from white caps, and/or include a correction for ozone (e.g., [43]–[46]). On the contrary, RH is not of general use in AC algorithms. Some results are also conditioned by the considered wavelengths so that they might be affected for sensors with different band sets. Moreover, dedicated analyses would be needed to estimate how uncertainties in ancillary data, particularly the concentrations of absorbing gases (e.g., O_3 or NO_2), might affect the subtle spectral features provided by hyperspectral missions, such as Plankton, Aerosol, Cloud, ocean Ecosystem (PACE) [47].

As explained in Section II, any perturbation occurring in the NIR bands has an impact across the spectrum for all variables (through the calculation of the aerosol radiance), while any perturbation occurring at one visible band can also have an impact at all bands if the black-pixel assumption is not valid and the iterative process is activated (this is true for 443, 555, and 670 nm through the L_w NIR correction, and possibly for other bands if used in the calculation of Chl-*a*). The algorithm contains LUTs (for aerosol and Rayleigh reflectance) and divergence points (associated with the selection of aerosol models), and some radiative contributions are affected by thresholds and saturation, like the calculation of the white cap and moderate glint radiances. Changes in ancillary data have an impact on the AC process in various, sometimes compensating, ways. All these elements make understanding the effects of variations in ancillary data particularly challenging and, in general, impede an analytic derivation of these effects. Based on simplifying assumptions, the development and analysis of (12), (13), or (15) go some way into explaining some of the observed behaviors but similar developments are not easily done for all cases. The present analysis relies on calculations performed globally across a year and therefore covers a representative sample of the large diversity (in the geometry of illumination/observation, water content, atmospheric, and meteorological conditions) surveyed by the satellite imagery so that the net effect of uncertainties in ancillary data could be documented. Focusing on R_{RS}, it can be observed that an increase in WS and PW is usually translated into an increase at all bands, while an increase in SLP tends to reduce R_{RS}. No clear trend can be ascertained when RH is varied. In the case of an increase in $[O_3]$, R_{RS} tends to increase for bands above 490 nm (most noticeably at 555 nm) but to decrease at 412–443 nm where ozone absorption is lowest.

Thus, it appears that R_{RS} might respond differently to variations in ancillary data, in time and space but also spectrally. The focus of this study is on the outputs of the AC but, for the sake of discussion, the impact of the variations observed on R_{RS} on the main OC derived product, Chl-*a*, is here briefly presented in terms of σ_{ens}. Chl-*a* is the standard NASA product obtained by a combination of a blue-to-green maximum-band-ratio algorithm and a band-difference algorithm (for oligotrophic regions) [48], [49]. The resulting map of σ_{ens} [Fig. 12(a)] does not obviously compare with the variations observed for R_{RS} [Fig. 2(c) and (d)], while it is more like a Chl-*a* average map with high values at high latitudes or in upwelling areas. For instance, while there is a local minimum for R_{RS} in the eastern equatorial Pacific cold tongue, there is a local maximum seen for Chl-*a* extending much further west. Also notable are the patterns of Chl-*a*'s σ_{ens} in the Southern Ocean that are much less intense than for R_{RS}, while it is consistently high in the northern high latitudes. The global median of σ_{ens} is 0.0034 mg m^{-3} with most values below 0.1 mg m^{-3} [Fig. 12(b)], while the median ratio of σ_{ens} and annually averaged Chl-*a* is 2.2%. The high range of σ_{ens}, largely associated with the high latitude northern hemisphere, is significantly contributed by variations in $[O_3]$ [Fig. 12(b)]. The global median of σ_{ens} when only $[O_3]$ is perturbed ($[O_3]$ case) is 0.0025 mg m^{-3} (1.6% in relative terms), while it is 0.0018 mg m^{-3} (1.1% in relative terms) when perturbing only the meteorological variables (MET case). This relatively large impact associated with $[O_3]$ is due to the inverse response observed for R_{RS} in the blue and green

bands (Fig. 8), all the more active in high latitudes with larger optical paths. Obviously, these results could be very different for other derived products, such as absorption or backscattering coefficients, and this example on Chl-*a* suggests that dedicated uncertainty propagation analyses would be needed for each form of bio-optical algorithms.

An important assumption of the study is that the spread within the ensemble data and/or the differences between the CERA and reference (NCEP/TOMS) data (with frequency distributions and median values given in Fig. 1 in the Supplementary Material) are representative of the uncertainties affecting the ancillary products. The former might be an underestimate [32], while the latter is typical of the differences that can exist between ancillary data distributed by various organizations. As the two products cannot be both close to the truth, their differences are related to the uncertainties of at least one of them. It is interesting to notice that the ensemble spread within the CERA data, σ_{ens}, and the RMS difference between the CERA and reference datasets, σ_{dif}, have important patterns in common (e.g., in the Southern Ocean and North Pacific for WS or SLP, in the subtropical region for PW and RH, a latitudinal gradient for $[O_3]$ …), which supports the idea that they offer a representative view of the relative geographical distribution of the ancillary data uncertainties, or at least allow a realistic sensitivity analysis on the AC (see [8] for a more complete discussion). These elements, associated with the application of the AC at a global scale for a full year, indeed suggest that this study encompasses a fairly comprehensive description of the influence of the ancillary data uncertainties on the OC output products. This being said, it is stressed that the results need to be considered with caution as the variations observed for the OC products are fully dependent on those associated with the ancillary data (either expressed as σ_{ens} or σ_{dif}) and that a similar analysis should be repeated with actual uncertainty estimates for the ancillary data. It is also acknowledged that the observed variations do not include contributions associated with the fairly coarse resolution (spatial and temporal) of the ancillary data (typically 1° and 6-h-to-daily). For instance, WS in coastal regions or in the wake of islands, or even NO_2 in coastal regions [14], show variations that are not well represented at these scales. Therefore, conducting similar sensitivity analyses at regional scales with appropriate datasets would be welcome. It is also recalled that the study focused exclusively on the effect of uncertainties in ancillary data, ignoring uncertainties associated with the way they are used in the algorithms (related to model errors). A typical example is significant uncertainty related to the conversion from WS to white cap coverage and radiance (e.g., [50]) that might be comparable to the uncertainty on WS.

A comment is due to the systematic differences between the CERA and reference datasets. Indeed, a change of ancillary dataset would require an update of the system vicarious calibration (SVC) coefficients [11], [51] that would remove the impact of systematic differences (or bias) between these data. It is, however, stressed that the systematic difference observed between CERA and reference data (δ_{dif}) accounts for only a part of the observed differences (expressed by σ_{dif}). More importantly, the location of the SVC site operating the Marine Optical Buoy (MOBY) close to the Hawaiian archipelago [52] corresponds to fairly low values of δ_{dif} for the meteorological variables and a negative value for $[O_3]$ (Fig. 5); using bilinear interpolation on the four grid points surrounding the buoy site, δ_{dif} is $+1.1$ m s^{-1}, 0 hPa, -2.3 kg m^{-2}, 0.9%, and -13 dobs for WS, SLP, PW, RH, and $[O_3]$, respectively. Therefore, a correction of the SVC coefficients due to a change in the source of the meteorological data would not correct for much larger differences seen elsewhere, e.g., in the Southern Ocean for WS and SLP, or in the tropics for PW and RH. In addition, these larger differences can either be positive or negative, so an update of the SVC coefficients could compensate for these differences only in some regions. This is typically observed for $[O_3]$: R_{RS} products processed with the CERA ozone data with updated SVC coefficients would be brought closer to the standard R_{RS} products obtained with TOMS data at the latitudes of MOBY, but their differences would further diverge at high latitudes. Actually, what is known about the patterns of uncertainties affecting ancillary data should be added as auxiliary information when documenting the location of SVC sites [53].

The distributions obtained for statistical parameters such as σ_{ens}, σ_{dif} and δ_{dif} for a full-year show distinct spatial patterns that consequently are often found in the OC output products. Considering the range of perturbations applied, WS and RH appear as the ancillary variables having the largest impact on the OC variables such τ_a and R_{RS}, with $[O_3]$ playing a role for bands with high absorption, such as 555 nm. In the variance space, the sum of variations observed in R_{RS} when only one ancillary variable is perturbed is close to the variations seen when all five variables are perturbed, which suggests that at first order, the effects are fairly uncorrelated. In general, the variations observed for R_{RS} are fairly low, representing a few % of the average signal, but they are by no means negligible; for instance, the median ratio of σ_{ens} and the annual average μ_{yr} is 2.8% at 555 nm, while the median ratio of σ_{dif} and μ_{yr} is 7.6% for the same band. When comparing with the natural variability expressed by σ_{yr}, the median ratio is in the interval 6.3%–12% for σ_{ens}, and 13.6%–32.9% for σ_{dif}.

In terms of recommendations, including the uncertainties associated with ancillary data when building uncertainty budgets for AC algorithms is certainly required, and for this, having uncertainty estimates for each ancillary datum would be useful. The distribution of representative ensemble datasets would already represent a noteworthy step in the right direction.

ACKNOWLEDGMENT

The Ocean Biology Distributed Active Archive Center (OB.DAAC) of the National Aeronautics and Space Administration (NASA), Greenbelt, MD, USA, is acknowledged for the distribution of the SeaWiFS level-1 data and ancillary files for NCEP and TOMS/TOVS data. The European Centre for Medium-Range Weather Forecast (ECMWF) is thanked for the availability of the CERA-20C ensemble data that allowed this research, and Dr. Bill Bell is thanked for his advice and support on using these data.

REFERENCES

[1] H. R. Gordon, D. K. Clark, J. L. Mueller, and W. A. Hovis, "Phytoplankton pigments from the Nimbus-7 Coastal Zone Color Scanner: Comparisons with surface measurements," *Science*, vol. 210, no. 4465, pp. 63–66, Oct. 1980.

[2] T. Platt, N. Hoepffner, V. Stuart, and C. Brown, Eds., "Why ocean colour? The societal benefits of ocean-colour technology," in *Reports of the International Ocean Colour Coordinating Group*, vol. 7. Dartmouth, NC, Canada: IOCCG, 2008.

[3] *Systematic Observation Requirements for Satellite-Based Products for Climate*, GCOS-154, Supplemental Details to the Satellite-Based Component of the Implementation plan for the Global Observing System for Climate in Support of the UNFCC, GCOS, Geneva, Switzerland, 2011.

[4] R. Hollmann *et al.*, "The ESA climate change initiative: Satellite data records for essential climate variables," *Bull. Amer. Meteorolog. Soc.*, vol. 94, pp. 1541–1552, Oct. 2013.

[5] C. J. Merchant *et al.*, "Uncertainty information in climate data records from Earth observation," *Earth Syst. Sci. Data*, vol. 9, no. 2, pp. 511–527, Jul. 2017.

[6] F. Mélin, Ed., *Uncertainties in Ocean Colour Remote Sensing* (Reports of the International Ocean Colour Coordinating Group), vol. 18. Dartmouth, NS, Canada: IOCCG, 2019.

[7] *Evaluation of Measurement Data—Guide to the Expression of Uncertainty in Measurements*, JCGM 100, Joint Committee for Guides in Metrology, Bureau International des Poids et Mesures, GUM, Chicago, IL, USA, 2008.

[8] P. De Vis, F. Mélin, S. Hunt, R. Morrone, M. Sinclair, and B. Bell, "Ancillary data uncertainties within the SeaDAS uncertainty budget," *Remote Sens.*, vol. 14, p. 497, Jan. 2022.

[9] G. Fu, K. Baith, and C. McClain, "SeaDAS: The SeaWiFS data analysis system," in *Proc. 4th Pacific Ocean Remote Sens. Conf.*, Qingdao, China, Jul. 1998, pp. 73–79.

[10] H. R. Gordon and M. Wang, "Retrieval of water-leaving radiance and aerosol optical thickness over the oceans with SeaWiFS: A preliminary algorithm," *Appl. Opt.*, vol. 33, no. 3, pp. 443–452, 1994.

[11] B. A. Franz, S. W. Bailey, P. J. Werdell, and C. R. McClain, "Sensor-independent approach to the vicarious calibration of satellite ocean color radiometry," *Appl. Opt.*, vol. 46, no. 22, pp. 5068–5082, Aug. 2007.

[12] Z. Ahmad *et al.*, "Atmospheric correction for NO_2 absorption in retrieving water-leaving reflectances from the SeaWiFS and MODIS measurements," *Appl. Opt.*, vol. 46, no. 26, pp. 6504–6512, 2007.

[13] M. Tzortziou, J. R. Herman, Z. Ahmad, C. P. Loughner, N. Abuhassan, and A. Cede, "Atmospheric NO_2 dynamics and impact on ocean color retrievals in urban nearshore regions," *J. Geophys. Res., Oceans*, vol. 119, no. 6, pp. 3834–3854, Jun. 2014, doi: 10.1002/2014JC009803.

[14] M. Tzortziou *et al.*, "Atmospheric trace gas (NO_2 and O_3) variability in South Korean coastal waters, and implications for remote sensing of coastal ocean color dynamics," *Remote Sens.*, vol. 10, no. 10, p. 1587, Oct. 2018, doi: 10.3390/rs10101587.

[15] P. Schneider, W. A. Lahoz, and R. van der A, "Recent satellite-based trends of tropospheric nitrogen dioxide over large urban agglomerations worldwide," *Atmos. Chem. Phys.*, vol. 15, no. 3, pp. 1205–1220, Feb. 2015.

[16] M. Wang, "Atmospheric transmittance of ocean color sensors: Computing atmospheric diffuse transmittance," *Appl. Opt.*, vol. 38, pp. 451–455, Jan. 1999.

[17] H. Gordon and D. Clark, "Clear water radiances for atmospheric correction of coastal zone color scanner imagery," *Appl. Opt.*, vol. 20, pp. 4175–4180, Dec. 1981.

[18] A. Morel and G. Gentili, "Diffuse reflectance of oceanic waters. III. Implication of bidirectionality for the remote-sensing problem," *Appl. Opt.*, vol. 35, no. 24, pp. 4850–4862, 1996.

[19] M. Wang, "Effects of ocean surface reflectance variation with solar elevation on normalized water-leaving radiance," *Appl. Opt.*, vol. 45, no. 17, pp. 4122–4128, 2006.

[20] A. Morel, D. Antoine, and B. Gentili, "Bidirectional reflectance of oceanic waters: Accounting for Raman emission and varying particle scattering phase function," *Appl. Opt.*, vol. 41, no. 30, pp. 6289–6306, 2002.

[21] D. A. Siegel, M. Wang, S. Maritorena, and W. Robinson, "Atmospheric correction of satellite ocean color imagery: The black pixel assumption," *Appl. Opt.*, vol. 39, no. 21, pp. 3582–3591, 2000.

[22] H. R. Gordon, "Atmospheric correction of ocean color imagery in the Earth Observing System era," *J. Geophys. Res.*, vol. 102, no. D14, pp. 17081–17106, 1997.

[23] Z. Ahmad *et al.*, "New aerosol models for the retrieval of aerosol optical thickness and normalized water-leaving radiances from the SeaWiFS and MODIS sensors over coastal regions and open oceans," *Appl. Opt.*, vol. 49, no. 29, pp. 5545–5560, 2010.

[24] S. W. Bailey, B. A. Franz, and P. J. Werdell, "Estimation of near-infrared water-leaving reflectance for satellite ocean color data processing," *Opt. Exp.*, vol. 18, no. 7, pp. 7521–7527, Mar. 2010.

[25] M. Stramska, "Observations of oceanic whitecaps in the north polar waters of the Atlantic," *J. Geophys. Res.*, vol. 108, no. C3, p. 3086, 2003, doi: 10.1029/2002JC001321.

[26] C. Cox and W. Munk, "Measurement of the roughness of the sea surface from photographs of the Sun's glitter," *J. Opt. Soc. Amer.*, vol. 44, no. 11, pp. 838–850, Nov. 1954.

[27] M. Wang, "The Rayleigh lookup tables for the SeaWiFS data processing: Accounting for the effects of ocean surface roughness," *Int. J. Remote Sens.*, vol. 23, no. 13, pp. 2693–2702, Jan. 2002.

[28] M. Wang, "A refinement for the Rayleigh radiance computation with variation of the atmospheric pressure," *Int. J. Remote Sens.*, vol. 26, no. 24, pp. 5651–5663, Dec. 2005.

[29] M. Kanamitsu *et al.*, "NCEP–DOE AMIP-II reanalysis (R-2)," *Bull. Amer. Meteorolog. Soc.*, vol. 83, no. 11, pp. 1631–1644, Nov. 2002.

[30] S. Saha *et al.*, "The NCEP climate forecast system reanalysis," *Bull. Amer. Meteorolog. Soc.*, vol. 83, no. 8, pp. 1631–1643, 2002.

[31] R. McPeters *et al.*, "Earth probe total ozone mapping spectrometer (TOMS) data products user's guide," in *NASA Technical Publication*. Greenbelt, MD, USA: NASA Goddard Space Flight Center, 1998, p. 64.

[32] P. Laloyaux *et al.*, "CERA-20C: A coupled reanalysis of the twentieth century," *J. Adv. Model. Earth Syst.*, vol. 10, no. 5, pp. 1172–1195, May 2018, doi: 10.1029/2018MS001273.

[33] O. A. Alduchov and R. E. Eskridge, "Improved Magnus form approximation of saturation vapor pressure," *J. Appl. Meteorol.*, vol. 35, no. 4, pp. 601–609, 1996.

[34] M. J. McPhaden *et al.*, "The tropical ocean-global atmosphere observing system: A decade of progress," *J. Geophys. Res. Oceans*, vol. 103, no. C7, pp. 14169–14240, Jun. 1998.

[35] J. Servain *et al.*, "A pilot research moored array in the tropical Atlantic (PIRATA)," *Bull. Amer. Meteorolog. Soc.*, vol. 79, no. 10, pp. 2019–2031, Oct. 1998.

[36] M. J. Brennan, H. D. Cobb, and R. D. Knabb, "Observations of Gulf of tehuantepec gap wind events from QuikSCAT: An updated event climatology and operational model evaluation," *Weather Forecasting*, vol. 25, no. 2, pp. 646–658, Apr. 2010.

[37] M. Wang, "Study of the Sea-viewing Wide Field-of-view Sensor (SeaWiFS) aerosol optical property data over ocean in combination with the ocean color products," *J. Geophys. Res.*, vol. 110, no. D10, 2005, Art. no. D10S06, doi: 10.1029/2004JD004950.

[38] M. Wang and S. Bailey, "Correction of sun glint contamination on the SeaWiFS ocean and atmosphere products," *Appl. Opt.*, vol. 40, no. 27, pp. 4790–4798, 2001.

[39] R. Frouin, M. Schwindling, and P.-Y. Deschamps, "Spectral reflectance of sea foam in the visible and near-infrared: *in situ* measurements and remote sensing implications," *J. Geophys. Res., Oceans*, vol. 101, no. C6, pp. 14361–14371, Jun. 1996.

[40] R. Guzzi and R. Rizzi, "Water vapor absorption in the visible and near infrared: Results of field measurements," *Appl. Opt.*, vol. 23, pp. 1853–1861, Jun. 1984.

[41] A. Smirnov *et al.*, "Maritime aerosol network as a component of aerosol robotic network," *J. Geophys. Res.*, vol. 114, Mar. 2009, Art. no. D06204, doi: 10.1029/2008JD011257.

[42] A. Smirnov *et al.*, "Maritime aerosol network as a component of AERONET—First results and comparison with global aerosol models and satellite retrievals," *Atmos. Meas. Techn.*, vol. 4, no. 3, pp. 583–597, 2011.

[43] C. P. Kuchinke, H. R. Gordon, and B. A. Franz, "Spectral optimization for constituent retrieval in case 2 waters I: Implementation and performance," *Remote Sens. Environ.*, vol. 113, no. 3, pp. 571–587, Mar. 2009.

[44] F. Steinmetz, P.-Y. Deschamps, and D. Ramon, "Atmospheric correction in presence of sun glint: Application to MERIS," *Opt. Exp.*, vol. 19, pp. 571–587, May 2011.

[45] R. Frouin and B. Pelletier, "Bayesian methodology for inverting satellite ocean-color data," *Remote Sens. Environ.*, vol. 159, pp. 332–360, Mar. 2015.

[46] Y. Fan *et al.*, "OC-SMART: A machine learning based data analysis platform for satellite ocean color sensors," *Remote Sens. Environ.*, vol. 253, Feb. 2021, Art. no. 112236.

[47] P. Werdell *et al.*, "The Plankton, Aerosol, Cloud, Ocean Ecosystem mission: Status, science, advances," *Bull. Amer. Meteorolog. Soc.*, vol. 100, pp. 1775–1794, Sep. 2019.
[48] J. E. O'Reilly and P. J. Werdell, "Chlorophyll algorithms for ocean color sensors–OC4, OC5 & OC6," *Remote Sens. Environ.*, vol. 229, pp. 32–47, Aug. 2019.
[49] C. Hu, Z. Lee, and B. Franz, "Chlorophyll a algorithms for oligotrophic oceans: A novel approach based on three-band reflectance difference," *J. Geophys. Res., Oceans*, vol. 117, no. C1, Jan. 2012, Art. no. C01011, doi: 10.1029/2011JC007395.
[50] S. E. Brumer *et al.*, "Whitecap coverage dependence on wind and wave statistics as observed during SO GasEx and HiWinGS," *J. Phys. Oceanogr.*, vol. 47, no. 9, pp. 2211–2235, Sep. 2017.
[51] G. Zibordi *et al.*, "System vicarious calibration for ocean color climate change applications: Requirements for *in situ* data," *Remote Sens. Environ.*, vol. 159, pp. 361–369, Mar. 2015.
[52] D. K. Clark, H. R. Gordon, K. J. Voss, Y. Ge, W. Broenkow, and C. Trees, "Validation of atmospheric correction over the oceans," *J. Geophys. Res.*, vol. 102, no. D14, pp. 17209–17217, Jul. 1997.
[53] G. Zibordi and F. Mélin, "An evaluation of marine regions relevant for ocean color system vicarious calibration," *Remote Sens. Environ.*, vol. 190, pp. 122–136, Mar. 2017.

Frédéric Mélin received the Dipl.-Ing. degree from the Ecole Nationale Supérieure de l'Aéronautique et de l'Espace, Toulouse, France, in 1995, and the Ph.D. degree from the Université Paul Sabatier, Toulouse, in 2003.

He was a Research Assistant in the field of physical oceanography with the Jet Propulsion Laboratory, California Institute of Technology, National Aeronautics and Space Administration, Pasadena, CA, USA, from 1995 to 1997. Since 1998, he has been with the Joint Research Centre, European Commission, Ispra, Italy, where his research focuses on the determination of atmospheric and marine optical properties based on optical remote sensing and the determination of their uncertainties. His research interests include the use of satellite data, with an emphasis on ocean color, together with models, for the study of marine biogeochemical cycles.

Paolo Colandrea received the M.Sc. degree *(cum laude)* in physical oceanography from the Parthenope University of Naples, Naples, Italy, in 1997. His M.Sc. thesis was on MW remote sensing of the ocean.

Since 1998, he has been working in private companies in the field of satellite remote sensing, participating in several national and international projects funded by the main European space agencies, gaining a wide experience in several fields of satellite remote sensing, including land, atmosphere, and ocean monitoring, and relative applications and services with both optical and MW sensors. He has been also involved in the development of the PRISMA mission, the first European hyperspectral satellite funded by the Italian Space Agency, Rome, Italy.

Pieter De Vis received the B.Sc. and M.Sc. degrees in physics and astronomy from Ghent University, Ghent, Belgium, in 2010 and 2012, respectively, and the joint Ph.D. degree from Ghent University and University of Canterbury, Christchurch, New Zealand, in 2016.

He worked in astronomy, where he focused on cosmic dust in galaxies, a topic that shares many concepts with Earth observation, particularly with how light travels through the atmosphere. He has been with the Climate and Earth Observation Group, National Physical Laboratory, Teddington, U.K., since 2019, where his expertise lies in atmospheric correction, the propagation of uncertainties through a measurement function, and uncertainties in model fitting. He is an experienced programmer and has developed many modular python tools for both internal and external use. He has applied this expertise to quantify uncertainties in various fields, including ocean color, greenhouse gases, and surface reflectances.

Samuel E. Hunt received the master's degree in physics from the University of Durham, Durham, U.K., in 2014.

He was a Trainee with European Space Agency, European Space Research and Technology Centre, Noordwijk, The Netherlands. He was a part of the Sentinel-3/OLCI Performance Team. In 2016, he joined the National Physical Laboratory, Teddington, U.K., where he is currently a Research Scientist focusing on the satellite Earth Observation metrology. His work aims to improve the quality of and confidence in satellite Earth observations, using insights from metrology.